Why MagNet: Quantifying the Complexity of Modeling Power Magnetic Material Characteristics

Diego Serrano [ID], Haoran Li [ID], *Graduate Student Member, IEEE*, Shukai Wang [ID], *Graduate Student Member, IEEE*, Thomas Guillod [ID], *Member, IEEE*, Min Luo [ID], *Senior Member, IEEE*, Vineet Bansal, Niraj K. Jha [ID], *Fellow, IEEE*, Yuxin Chen [ID], *Senior Member, IEEE*, Charles R. Sullivan [ID], *Fellow, IEEE*, and Minjie Chen [ID], *Senior Member, IEEE*

Abstract— This article motivates the development of sophisticated data-driven models for power magnetic material characteristics. Core losses and hysteresis loops are critical information in the design process of power magnetics, yet the physics behind them is not fully understood or directly applicable. Both losses and hysteresis loops change for each magnetic material and depend heavily on electrical operating conditions (e.g., waveform, frequency, amplitude, and dc bias), mechanical properties (e.g., pressure and vibration), temperature, and geometry of the magnetic components, and in a nonlinear and coupled fashion. Understanding the complex and intertwined relationship these factors have on core loss is important for the development of accurate models and their applicability and limitations. Existing studies on power magnetics are usually developed based on a small amount of data and do not reveal the full magnetic behavior across a wide range of operating conditions. In this article, based on a recently developed large-scale open-source database—*MagNet*—the core losses and hysteresis loops of Mn–Zn ferrites are analyzed over a wide range of amplitudes, frequencies, waveform shapes, dc bias levels, and temperatures, to quantify the complexity of modeling magnetic core losses, amplitude permeability, and hysteresis loops and provide guidelines for modeling power magnetics with data-driven methods.

Index Terms—B–H loop, core loss, data-driven methods, data visualization, hysteresis, open-source database, power magnetics, soft ferrites.

Diego Serrano, Haoran Li, Shukai Wang, Vineet Bansal, Niraj K. Jha, and Minjie Chen are with the Department of Electrical and Computer Engineering and the Andlinger Center for Energy and the Environment, Princeton University, Princeton, NJ 08540 USA (e-mail: ds9056@princeton.edu; haoranli@princeton.edu; sw0123@princeton.edu; vineetb@princeton.edu; jha@princeton.edu; minjie@princeton.edu).

Thomas Guillod and Charles R. Sullivan are with the Dartmouth College, Hanover, NH 03755 USA (e-mail: thomas.ph.guillod@dartmouth.edu; charles.r.sullivan@dartmouth.edu).

Min Luo is with the BASiC Semi, 518000 Zurich, Switzerland (e-mail: m.luo@ieee.org).

Yuxin Chen is with the Department of Statistics and Data Science, Wharton School, University of Pennsylvania, Philadelphia, PA 19104 USA (e-mail: yuxinc@wharton.upenn.edu).

Color versions of one or more figures in this article are available at https://doi.org/10.1109/TPEL.2023.3291084.

Digital Object Identifier 10.1109/TPEL.2023.3291084

I. Introduction

MAGNETIC components perform important functions in power electronics in many ways. Inductors and coupled inductors are required for regulation, to ensure resonant operation, and to achieve soft switching or soft charging. Transformers are needed to provide galvanic isolation and fixed gains. Different magnetic components are required for each application and operating condition. The future development of in-package and on-chip magnetics and magnetics for automotive, industrial, medical, and robotics applications makes a precise understanding of magnetic materials across wide operation ranges critical [1], [2], [3], [4].

The design of magnetics components is challenging and often an iterative process because of the large selection of winding structures (winding technology, number of turns, and arrangement) and core options (material, shape, and size) to choose from. Accurate models for windings exist [5], [6], [7], but accurate models for the behavior of magnetic materials are limited. Parameters, such as permeability, saturation level, or core losses, are heavily influenced by electrical, mechanical, and thermal conditions [8], [9].

The most important characteristic of magnetic materials is the relation between the flux density, $B(t)$, and the magnetic field strength, $H(t)$. This relation is usually described as a B–H hysteresis loop. An example of the static hysteresis curve is shown in Fig. 1(a) [10]. Commonly used design parameters, such as amplitude permeability, saturation level, or core losses, can be obtained from the B–H loop. Since the B–H loop changes drastically with excitation waveform and temperature, core loss and amplitude permeability are also affected. Typically, hysteresis loops are included in datasheets for extreme peak flux density, low frequency, and a few temperatures only.

Amplitude permeability, defined as the ratio between the peak-to-peak values of B and H, can be used to estimate the large-signal inductance of ungapped magnetic components. Although the inductance is mainly given by the gap in general, the permeability of the core might be needed for high-frequency inductors, where permeability is low and a gap is not required, to estimate the inductance of chokes, or to calculate the magnetizing current in transformers, which might impact soft-switching conditions in some cases. In datasheets, the amplitude permeability is usually given for a few sinusoidal excitations
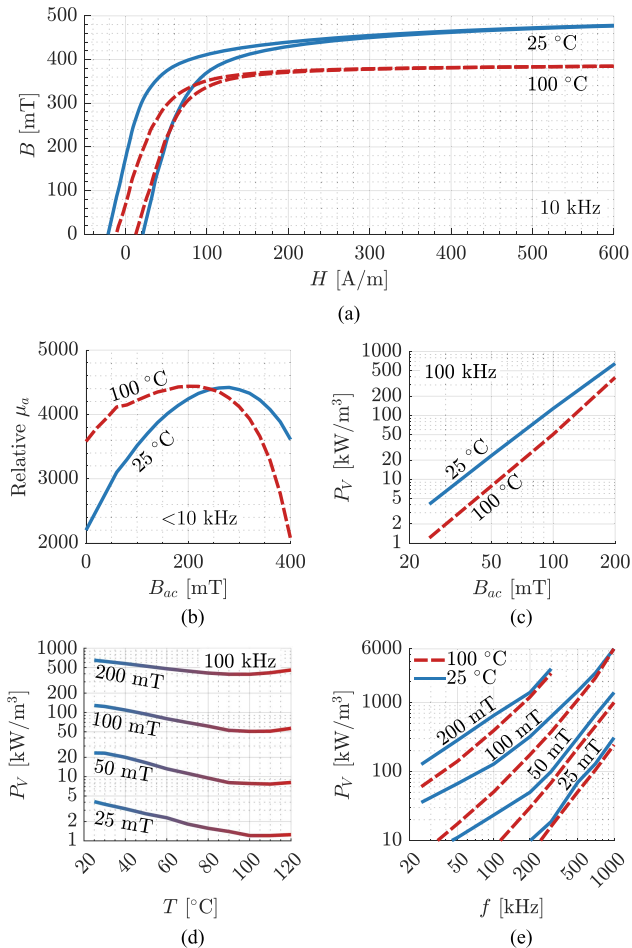
Fig. 1. Relevant information for the material N87 [10], from the manufacturer's software [11]. (a) B–H loop for a large excitation at 10 kHz at 25 °C and 100 °C. (b) Amplitude permeability for low-frequency excitations. (c) Volumetric core loss (P_V) as a function of peak flux density. (d) P_V as a function of temperature. (e) P_V as a function of frequency.

only [see Fig. 1(b)]. Generally, the other plots are dedicated to the permeability for very small B swings. In this article, the operating conditions affecting the amplitude permeability are investigated to assess whether the datasheet information is sufficient.

Core loss can be obtained from volumetric energy loss per cycle (the area inside the B–H loop). Core losses can limit the maximum frequency and flux density that magnetic components can handle. Estimation of core losses is also complex and cannot be obtained from datasheet parameters as usually only a few curves for core loss for sinusoidal waveforms are provided. Fig. 1(c)–(e) shows typical curves used to estimate core loss from the datasheet. In a few cases, manufacturers provide more data points by other means, such as specific software tools [11], but they are still limited to sinusoidal excitations without dc bias. To make matters worse, core losses are also impacted by the size and geometry of the core, as the magnetic field inside the core can be unevenly distributed, particularly at high frequencies [12], [13], [14].

Traditional datasheets cannot describe the behavior of magnetic materials under a mix of numerous realistic operating conditions. Multidimensional interpolations and extrapolations

are usually needed, which may introduce large errors, especially given the scarce data provided. A lot of progress has been made in the development of models for magnetic materials, yet, to date, analytical models cannot effectively cope with all these multiphysics multidimensional effects [15]. Physical models, although broadly able to explain the origins of core losses [12], [16], [17], [18], cannot yield accurate estimates for all circumstances yet, and analytical models (physics-based or empirical) are intended for only specific sets of operating conditions. Traditional studies on power magnetics usually start by separating many different impact mechanisms (e.g., waveform, temperature, and dc bias) but focus on one or a few mechanisms only. In this article, we demonstrate that modeling each individual factor independently may not result in a unified model with sufficient accuracy and generality and cannot lead to an accurate magnetic design tool. A sophisticated modeling framework that is powerful enough to capture many factors and their correlated impact is necessary to fully replicate the behaviors of magnetic materials and provide useful guidelines.

The main contributions of this article are: 1) quantifying and visualizing a large database of measurements to determine how different factors affect magnetic material behavior using the Mn–Zn ferrite material N87 as an example; 2) reviewing the literature for each one of the parameters affecting the behavior B–H loops and core losses; and 3) using the data to demonstrate the coupling between the different parameters affecting core losses. The purpose of this article is to motivate further research into more sophisticated and complete models for power magnetic materials and provide data to contrast existing and new models. Recently, models based on machine learning are being explored. The primary focus of [19], [20], and [21] is to model core loss and B–H loops using neural networks. Other recent examples of models based on neural networks accounting for various parameters include [15], with the added capability of modeling winding loss, and [22], for data with dc bias. In [23], neural networks are used not only to model inductors but also to optimize their design. Note that no new data-driven or physical-based model is introduced in this article.

The rest of this article is structured as follows. Section II presents the methodology used to acquire and process the data. In Section III, the vast amount of data is evaluated and visualized, discussing each of the key factors affecting the magnetic behaviors, including flux density, frequency, waveform shape, dc bias, temperature, core geometry, and core material. The effects of combining several parameters together are discussed in Section IV. Finally, Section V concludes this article.

II. DATA PREPARATION

One major obstacle for data-driven models of magnetic materials is that only a small amount of data is available in vendors' datasheets. A large-scale open-source power magnetics database—*MagNet*[1]—has been constructed recently to provide a common ground for data-driven characterization for power magnetics [25]. The data presented in this article are a subset
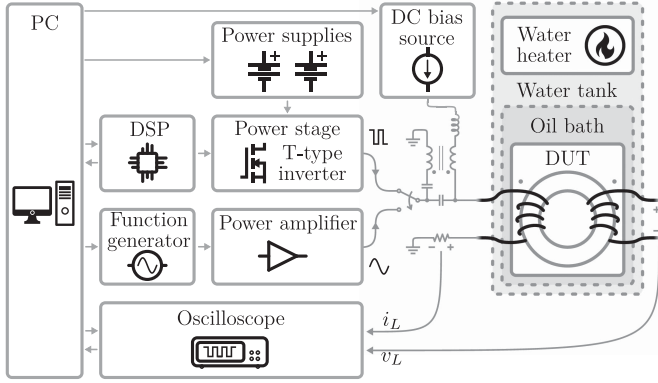
[1]Mag-Net Website: https://mag-net.princeton.edu/ [24]

Fig. 2. Block diagram of the automated setup highlighting how the different equipment is interconnected.

Fig. 3. Waveform shapes together with the definition of the duty cycles used throughout this article.

Fig. 4. Range for the tests for the B_{ac}, f, and H_{dc} variables.

of the MagNet database. This subset is selected to showcase the effects that different variables have on magnetic behavior in a range of peak flux density and frequency conditions. Nevertheless, data for more practical combinations of temperature, dc bias, waveform shape, and frequency are also available in the database. Details about this database and its construction are provided in a separate paper [20]. For completeness, the setup used to obtain the measurements and the methods to process the data are briefly included in the following subsections.

A. Hardware Setup

The two-winding method (also referred to as the V–I method or the voltamperometric method) is the most common procedure for B–H loop and core loss characterization [26], [27], [28], [29], [30], [31], [32], [33]. Two separated windings are used; a voltage excitation is applied to the primary and its current is measured to obtain H. The voltage across the secondary winding is measured to obtain B. This method is capable of capturing B–H loops under arbitrary excitation waveforms but is sensitive to time delays between the voltage and current measurement. This delay and other sources of errors affecting this solution are detailed in the Appendix. This method is selected as data collection can be easily automated since the setup does not need to be modified for each operating condition tested.

Fig. 2 shows a block diagram of the experimental setup. The automation and synchronization of different instruments are managed by a Python script. The different parts of the setup are described below and are designed following the recommendations in [32], [33], and [34].

1) *Device under test (DUT):* For most of this article, a toroidal core of 34-mm outer diameter, 20.5-mm inner diameter, and 12.5-mm height (designated R34.0 × 20.5 × 12.5 by the manufacturer) of the material N87 from TDK is studied [10]. In MagNet, 142 871 voltage and current pairs of waveforms for different operating conditions are included for this core.

2) *Excitation:* The DUT is excited with sinusoidal two-level pulsewidth-modulated (PWM), and three-level PWM voltages, leading to sinusoidal, triangular, and trapezoidal
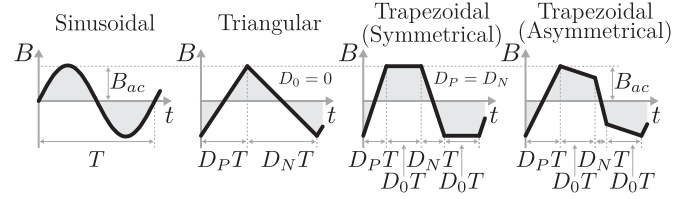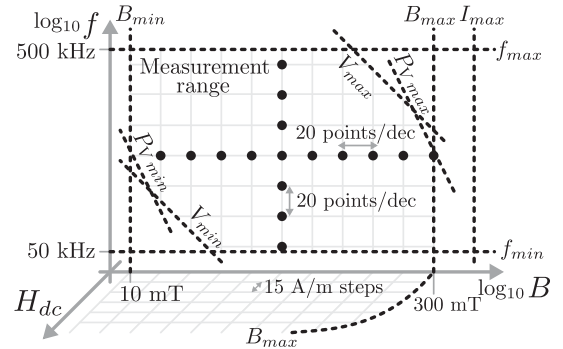
(symmetric and asymmetric) B waveforms (see Fig. 3). Sinusoidal waveforms are obtained using a power amplifier (Amplifier Research 25A250AM6) taking the reference from a function generator (RIGOL DG4102). A T-type inverter with GaN switches (GaN Systems GS66508B) supplied by two voltage sources (B&K Precision XLN60026) is used for triangular and trapezoidal excitation. The duty cycles, defined in Fig. 3, are iterated in 10% steps. A 100-µF 100-V film capacitor is placed between the power stage and the DUT to block the average voltage of the switching node to create asymmetrical PWM waveforms. For each waveform shape and temperature, the flux density and frequency are swept in the ranges and steps represented in Fig. 4.

3) *DC bias:* To bias the core, a direct current is injected into the primary winding, after the series capacitor. A transformer and a filter inductor are added to prevent the reflected voltage of the DUT from being applied to the current source (see Fig. 2). One winding of the transformer is connected to the excitation, while the other is connected between the excitation and the current source, canceling most of the ac voltage applied to the current source. Although the transformer could be omitted, it greatly reduces the voltage applied to the filter inductor, minimizing any current ripple. A voltage supply (Siglent SPD3303X-E) controlled in current mode is used to set the direct current. See [35] for details on the operation and construction of the dc bias circuitry. Fig. 4 also shows how the dc bias is iterated in the testing procedure. Note that a direct current is applied, defining H_{dc} rather than B_{dc}. B_{dc} is not reported in this article as there is no explicit relation between H_{dc}

and B_{dc} [33], and it cannot be calculated using the current measurement scheme.

4) *Data acquisition:* The measurements for the voltage and current waveform are acquired with an 8-bit oscilloscope (Tektronix DPO4054). 100 000 samples are saved for each test, with a total sample time of 80 μs. The bandwidth of the measurement is limited to 20 MHz to avoid excessive switching noise in triangular and trapezoidal waveforms due to the fast switching transitions. A low-capacitance passive probe (Tektronix P6139 A) and a coaxial shunt (T&M Research W-5-10-1STUD) are employed for voltage and current measurement, respectively.

5) *Temperature control:* Keeping a controlled temperature is critical since core losses are temperature dependent and core losses during testing heat up the core. The DUT is submerged in a mineral oil bath with a magnetic stirrer (INTLLAB) to keep the core and oil temperatures close. The oil bath is inside a water tank, and its temperature is controlled using a water heater (Anova AN400-US00). Measurements are collected at 25 °C, 50 °C, 70 °C, and 90 °C water temperature. In this article, the water temperature is used to report the core temperature, although there are small variations between the two temperatures during testing. This source of error is detailed in Appendix E.

There are limitations associated with the power stage/power amplifier. The voltage range for the tests is 1–50 V for sinusoidal waveforms and 5–80 V for PWM waveforms (see Fig. 4), which limits the flux density–frequency product of the data points measured, especially for extreme duty cycles. In addition, for sinusoidal waveforms, the power amplifier's linearity limits the voltage accuracy for large peak flux density, so data close to saturation are not available. For this reason, and the less severe voltage limitation, triangular data are the default excitation for this article. More details of the hardware setup are included in [20]. Moreover, a complete error analysis for this setup is provided in the Appendix.

B. Data Processing

The stored voltage and current measurements are processed to obtain the B and H waveforms and other parameters of interest (f, B_{ac}, D_P, D_N, H_{dc}, and P_V) in the following order.

1) *Data downsampling:* To compress the data, the measurements are downsampled from 100 000 to 10 000 samples per test using a boxcar averaging algorithm, which simply takes the average of consecutive ten samples. This reduction in data size increases the effective vertical resolution of the measurement at the expense of horizontal resolution [27].

2) *Fundamental frequency:* There might be a slight difference between the commanded frequency for the equipment and the actual frequency of the signal applied. With a sampling time of 8 ns and 10 000 samples, the resolution of fast Fourier transform (FFT) is only 12.5 kHz, rendering the FFT imprecise to calculate the fundamental frequency. Instead, the power spectral density of the signal is estimated using Welch's method [36]. The highest peak in
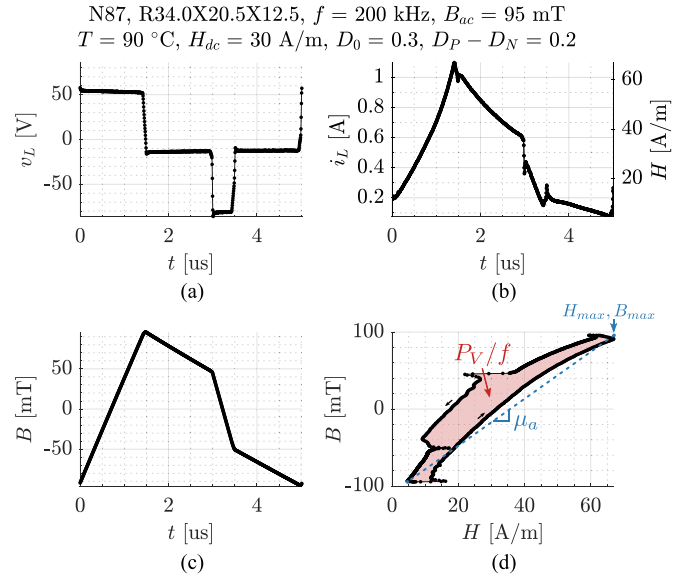

Fig. 5. Processed measurements for a random asymmetric trapezoidal waveform. (a) Measured voltage. (b) Measured current and magnetic field intensity. (c) Flux density. B_{dc} is not included. (d) B–H loop highlighting P_V and μ_a, as defined in (5).

the power spectral density near the commanded frequency corresponds to the fundamental frequency of the excitation signals.

3) *Single-cycle voltage and current:* Since the total sampling time is fixed to 80 μs, a different number of switching cycles are captured depending on the frequency of the excitation. The size of the database is further reduced by extracting a single-cycle waveform based on the detected fundamental frequency. To do so, the measured voltage and current waveforms are split into the different switching cycles sampled. These cycles are interpolated into 1024 samples per cycle, and then, the average waveform of the different switching cycles is obtained. To avoid artifacts, data are discarded based on the similitude of different cycles. More technically, when either the voltage or current waveform error, as defined by the following equation, is above 10%, the data point is discarded:

$$\text{error} = \frac{\sum_{i=1}^{N_{\text{cycles}}} \sum_{n=1}^{1024} \left(A_{i,n\,\text{meas}} - A_{n\,\text{averaged}}\right)^2}{N_{\text{cycles}} \sum_{n=1}^{1024} A_{n\,\text{averaged}}^2} \quad (1)$$

where $A_{i\,\text{meas}}$ is the measured voltage or current waveform of the ith cycle, A_{averaged} is the resulting voltage or current waveform after averaging, and n is the sample. Fig. 5(a) and (b) shows one example of the resulting single-cycle voltage and current waveforms. Any dc offset in the voltage waveform is removed.

4) *$\boldsymbol{B}$ and $\boldsymbol{H}$ waveforms:* The rest of the parameters are obtained from the single-cycle voltage and current. Flux density is calculated by integrating the voltage using (2). However, the initial value of B cannot be obtained with this method since the voltage is not captured from the time that the excitation is first applied (as in [28]) but only on

steady-state conditions. Because of this limitation, in this article, B is defined so that its average value B_{dc} is 0, even for data with $H_{dc} \neq 0$

$$B^*(t) = \frac{1}{A_e \cdot n_2} \int v_L(t)\, dt; \ B(t) = B^*(t) - \overline{B^*} \quad (2)$$

where B^* is the flux density before its average value is removed. The data are reported as a function of the amplitude of $B(t)$, B_{ac}, defined as $(B_{max} - B_{min})/2$. Magnetic field strength H is obtained from current measurements using the following equation:

$$H(t) = \frac{n_1}{l_e} i_L(t), \quad H_{dc} = \overline{H}. \quad (3)$$

H_{dc} is defined as the average of $H(t)$ rather than as $(H_{max} + H_{min})/2$.

Effective parameters l_e, A_e, and V_e are obtained from the manufacturer's datasheet. An example of B and H waveforms pairs is shown in Fig. 5(b) and (c), respectively. Note that B and H are obtained from the voltage and current measurements, and, as such, any measurement error is directly reflected in the B–H loop. More details on the sources of error are provided in the Appendix. Also, these B and H represent the mean magnitude of the B and H fields inside the core, but the fields are not homogeneous across the cross-sectional area, as explained in Section III-H.

5) *Core loss:* Core losses are obtained directly from the average of the product of the voltage and current waveforms [30]. For volumetric core loss, the obtained value is divided by the effective volume of the core V_e. Alternatively, volumetric core losses per cycle can be calculated from the integral of $H(t)$ over $B(t)$ [37] [see Fig. 5(d)]

$$P_V = \frac{f}{V_e} \int_0^{\frac{1}{f}} v_L(t) \cdot i_L(t)\, dt = f \oint H(B)\, dB. \quad (4)$$

6) *Amplitude permeability:* Amplitude permeability, together with the number of turns, can be used to obtain the relation between volt–second and current ripple in inductors. It is directly calculated from the peak to peak B and H, as follows:

$$\mu_a = \frac{B_{max} - B_{min}}{H_{max} - H_{min}}. \quad (5)$$

Note that the peak in B and H can be reached at slightly different times. As a result, the H_{max}, B_{max} point in the B–H plot might not be a point of the B–H loop itself [see Fig. 5(d)].

Further details on the postprocessing of the data, such as the calculation of the duty cycles, are available in [24]. Throughout the rest of this article, B–H loops, volumetric core loss, and amplitude permeability are visualized and studied under different operating conditions and external factors. Sometimes, the data do not form a perfect grid due to a small deviation of commanded B_{ac}, f, H_{dc}, and duty cycles from the measured values. To properly depict volumetric core loss and amplitude permeability as a function of other variables, interpolation is required. A linear interpolation is applied to $\log(B_{ac})$ and $\log(f)$, duty cycle, H_{dc},

and temperature for $\log(P_V)$ and $\log(\mu_a)$, after a Delaunay triangulation of the points. Interpolation is reliable if enough data points are collected to capture the trends. The data are not extrapolated because patterns and trends might change.

III. COMPLEXITY OF POWER MAGNETICS MODELING

In this section, the individual effect of waveform shape, dc bias, temperature, core size, and material in B–H loops, core losses, and permeability are investigated against frequency and amplitude using the extensive data in MagNet. Variables are introduced one by one aiming to narrow down the problem, and later, in Section IV, combined effects are discussed.

A. Frequency and Peak Flux Density in Sinusoidal Waveforms

At low frequencies, the quasi-static hysteresis is the dominant effect determining the B–H relationship. Physics-based microscopic models, such as the one presented in [12], are sometimes less practical than empirical models. Commonly used models for B–H loops include the Preisach model, derived from the theory in [38], and the Jiles–Atherton model [39]. A detailed description of common models is included in [40]. Dynamic models are also studied; for instance, an empirical method parameterized with measurements is described in [41]. Methods based on neural networks intended for low-frequency fields or sinusoidal excitations are also proposed in [42] and [43].

Fig. 6 provides an example of measured B–H loops for sinusoidal waveforms at increasing flux density and frequency. In general, peak flux density has a significant impact on the area of the loop and affects amplitude permeability. Frequency makes B–H loops have a more ellipsoidal shape with respect to the static hysteresis curves, while barely changing the amplitude permeability.

To visualize the behavior of core losses for sinusoidal waveforms of different frequencies and peak flux densities, Fig. 7(a) presents the data extracted from the MagNet database. Fig. 7(b) and (c) shows the same data in the form that is commonly presented in datasheets. The volumetric core loss for sinusoidal excitations is typically estimated using the Steinmetz equation [44], $P_V = k \cdot f^\alpha \cdot B_{ac}^\beta$, where the Steinmetz parameters, k, α, and β are constants that can be obtained by curve-fitting data for each material and f and B_{ac} are normalized to 1 Hz and 1 T, respectively. However, this simple yet effective equation has known limitations: it is only applicable to sinusoidal excitations; it is not accurate across wide frequencies [44], [45]; and its accuracy is largely influenced by the data and methods used to extract the Steinmetz parameters. To better understand its accuracy, the measured core losses can be compared to the prediction using the Steinmetz equation when k, α, and β are selected to best fit the measured data (i.e., minimize the total mean square error between the core loss of the complete set of sinusoidal measurements and the predicted loss [46]). Fig. 8 shows the ratio between the predicted and measured losses. This plot highlights how core losses deviate from a simple power law fitting for pure sinusoidal excitations, with errors above 20% in certain B–f regions. Note that part of this variation can be the result of small changes in the temperature of the core during
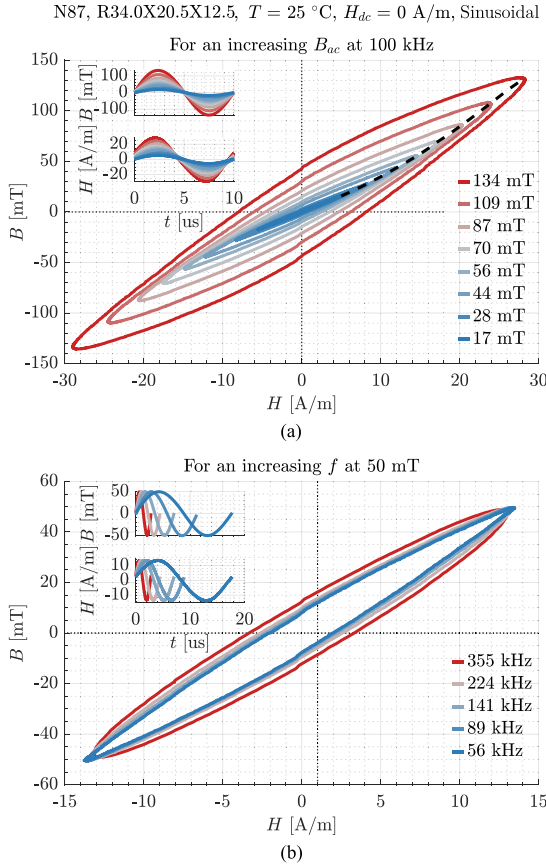
(a)

(b)

Fig. 6. Measured B–H loops for sinusoidal excitation at 25 °C without dc bias. (a) For different flux density amplitudes at 100 kHz. The peak B and H for all waveforms are joined with the discontinuous line to show the change in amplitude permeability. (b) For different frequencies at 50 mT. The voltage waveforms are not perfect sinewaves, especially at high flux density due to the use of a power amplifier. Only measurements with low THD ($<5\%$) in the voltage waveform are included to avoid the effects of distortion. Moreover, only data at relatively low $f \cdot B_{ac}$ are available due to the limited excitation voltage.

testing, as explained in Appendix E. More advanced models for core losses can be devised; a common approach is to separate the loss into different components (e.g., hysteresis loss, eddy current loss, relaxation loss, and residual loss) based on the physical phenomena responsible for each one [12], [16], [18], [37], [41], [46], [47], [48], [49]. The database could be used to fit or evaluate these methods.

The data in MagNet can also be processed to obtain amplitude permeability under different operating conditions. Fig. 9 shows the amplitude permeability in the f–B_{ac} plane for the N87 material at 25 °C for sinusoidal excitation. In a large portion of the measurement range, frequency does not impact the permeability substantially, while peak flux density does. These measurements show good agreement with the datasheet information in Fig. 1(b) in the 60–300 kHz range, showing that the datasheet information might be enough to capture μ_a for sinusoidal excitations.

B. Effect of Waveform Shape

Most magnetics in power electronics are excited by sinusoidal or PWM voltage ($\propto dB/dt$) [16], [31], [33], [37], leading to distorted sinusoidal, triangular, trapezoidal, or piecewise linear
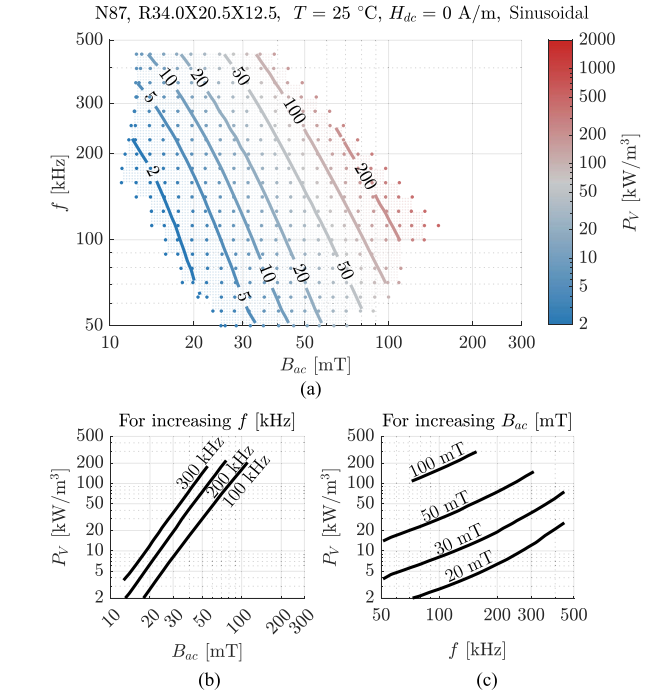

(a)

(b)

(c)

Fig. 7. Volumetric core losses for sinusoidal excitations at 25 °C without dc bias for data with THD$|_V < 5\%$. (a) As a function of B_{ac} and f (termed f–B_{ac} plane). Each dot is a measured value. The contours are based on the interpolation of the measurements. (b) For various frequencies as a function of B_{ac}. (c) For various B_{ac} as a function of f.
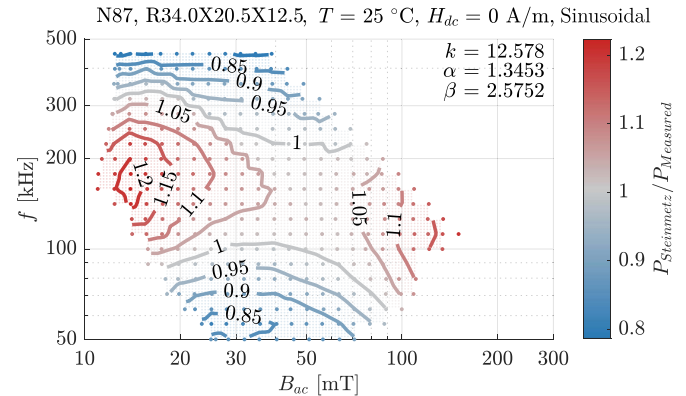

Fig. 8. Variation of the core losses between the prediction using the Steinmetz equation and the measurements. The Steinmetz parameters are obtained using the least-squares method for $\log_{10}(P_V)$ considering all the measured points (dots in the plot). A larger deviation would be obtained if other sets of Steinmetz parameters were used.

current ($\propto H$). In this section, we begin the examination of the impact of waveform shape by considering data for triangular $B(t)$ with 50% duty cycle. Fig. 10 shows the measured B–H loops for these waveforms, which are noticeably different from the sinusoidal measurements in Fig. 6, especially because of sharp changes in $H(t)$ when $B(t)$ reaches its peak. These peaks are affected by the transition speed of the voltage excitation (dv/dt), as explained in the next section.

For 50% duty cycle, core losses are shown in Fig. 11. At first glance, the results do not differ much from the sinusoidal
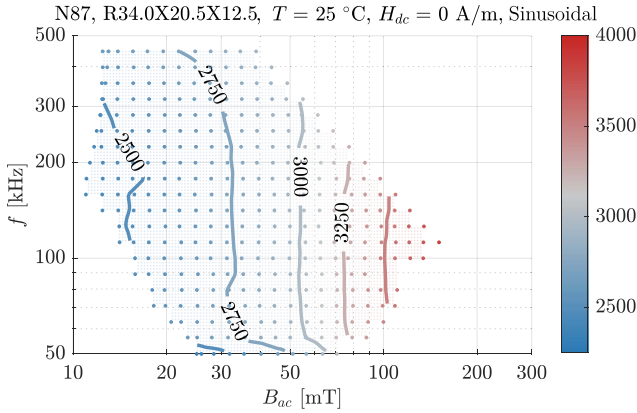
Fig. 9. Relative amplitude permeability (5) as a function of B_{ac} and f for sinusoidal excitations without dc bias at 25 °C. Interpolation is used to graph the contour plots.

Fig. 11. Core losses for a triangular 50% duty cycle excitation at 25 °C without dc bias as a function of B_{ac} and f. The contour is based on the interpolation of the measurements (each dot).
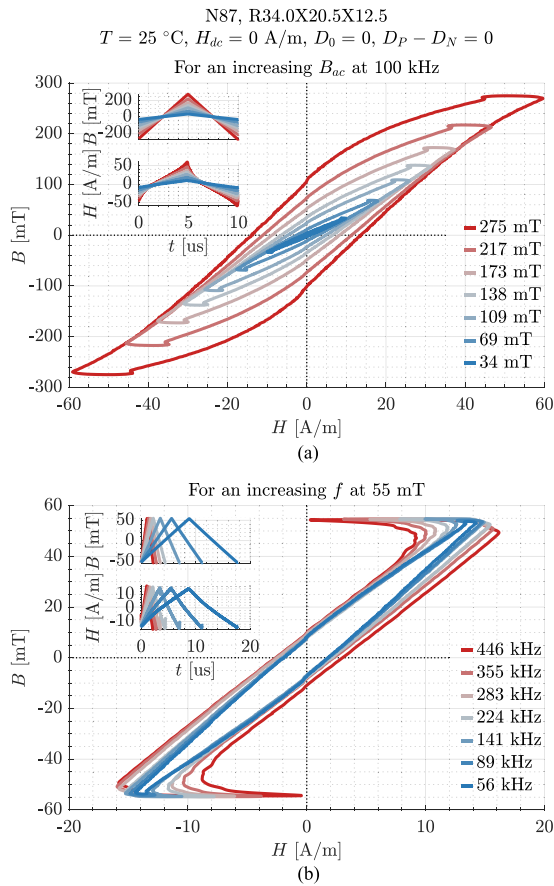

Fig. 10. Measured $B-H$ loops for triangular 50% duty cycle excitations at 25 °C without dc bias. This plot is used as a reference for comparison with other $B-H$ loops throughout this article. (a) For different flux density amplitudes at 100 kHz. (b) For different frequencies at 55 mT.

Fig. 12. Relative amplitude permeability as a function of B_{ac} and f for a triangular excitation with 50% duty cycle without dc bias at 25 °C.

reported μ_a, but in most cases, the peak does not change $B_{\max}$ or $H_{\max}$. Only data where ringing does not affect the reported μ_a are plotted in this article. Frequency has a larger effect in triangular waveforms as compared to sinusoidal waveforms (see Fig. 9), but the main behavior is still governed by the relation between B_{ac} and μ_a given in the datasheet [see Fig. 1(b)].

C. Impact of dv/dt During the Switching Transition

The measurement setup is not error-free. Parasitic capacitances, especially winding and core capacitance, influence the measured waveforms. Further discussion on the capacitances that play a role in the error is included in Appendix C. The significant challenge with the winding capacitance is that it is affected by the core itself. Due to the extremely large dielectric constant of the core (ϵ_r in the range of 10^5 [14], [50]), its contribution to total capacitance should not be ignored. The core provides a path with high capacitance and some resistance, affecting the winding capacitance [51], [52]. When a square voltage is applied to the DUT, a large current spike charges/discharges that capacitance during the transition, which alters the total current measured.

ones (see Fig. 7), showing that the power law behavior is still dominant, but again, contour lines are not straight. Note that the additional $B-H$ loop area due to fast switching transitions can affect these results.

Finally, Fig. 12 shows the relative amplitude permeability for 50% duty cycle triangular waveforms. The ringing in $H(t)$ during the switching transitions could affect the accuracy of the
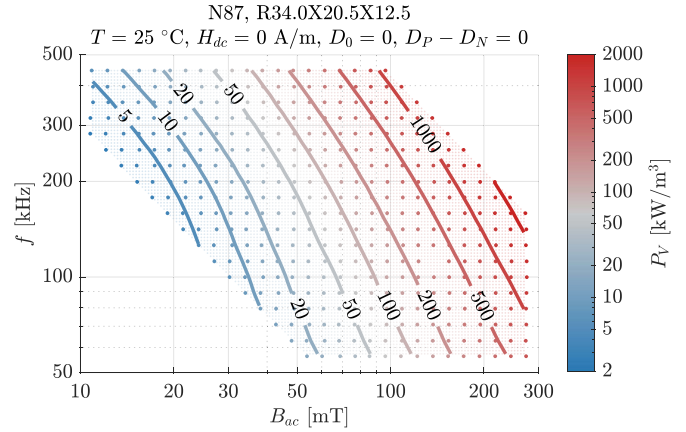
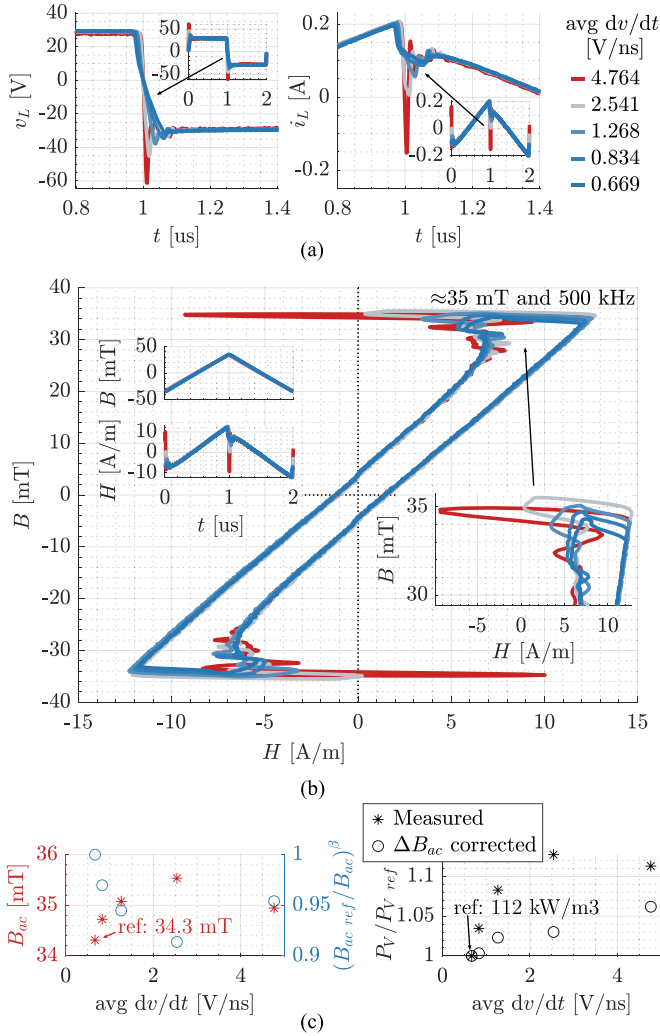Fig. 13. Effect of dv/dt tested with triangular 50% duty cycle excitation at 25 °C without dc bias. (a) Zoom of the voltage and current of the DUT with the full waveform as an inset. (b) B–H loops, including a zoom where the peak is better observed. (c) Calculated B_{ac} and ratio used to compensate the losses. (d) Measured losses and losses corrected for B_{ac}, normalized to the test with the lowest dv/dt. The effect of this small variation in B_{ac} in losses for $\beta = 2.5752$ is included to clarify that there is some impact associated with dv/dt in the B–H loop.

Fig. 14. Measured B–H loops for triangular waveforms of different duty cycles at 25 °C, 100 kHz, and 55 mT without dc bias.

This problem is exacerbated when employing GaN switches, due to the fast dv/dt achievable. Since H is calculated directly from the current measurement using (3), this current spike is reflected on the B–H loop. This effect has not been addressed in detail in the literature but was briefly discussed in [33].

The influence of dv/dt on the calculated B–H loop is hard to quantify for all the possible scenarios. Here, a comparison for a given operation point is provided. Since the waveforms are more severely affected at higher frequencies [see Fig. 10(b)], 500 kHz is selected as the frequency for the test. In this test, the switching speed is changed by loading the switching circuit with different external inductors, which increases the available current during the transition for zero-voltage switching (ZVS). The dead time is set to 100 ns and the input voltage is held constant, although the voltage applied to the DUT changes slightly because of the voltage drop in the power stage. Fig. 13(a) shows voltage and
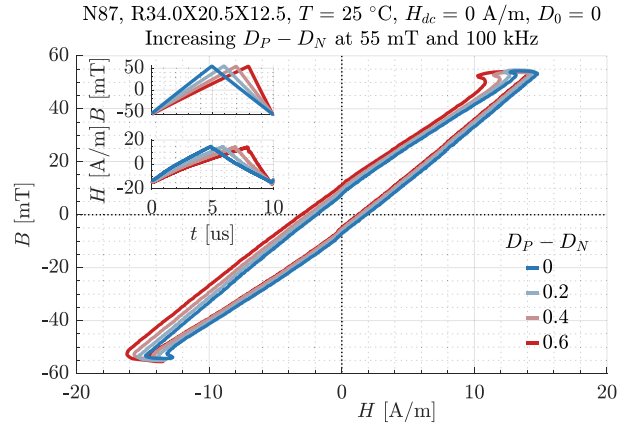
current, where the effect of the transition is highlighted. The measured current peaks because of dv/dt, and these peaks are also reflected in the B–H loops [see Fig. 13(b)], resulting in a change in the loop area. The total contribution of this effect to losses is also hard to quantify because the voltage waveform is modified by the ZVS transition and the total load current, leading to slightly different B_{ac}. The ratio between the losses of each waveform and the losses at the lowest dv/dt among them is shown in Fig. 13(c). B_{ac} also changes, but even after accounting for its effect by assuming losses proportional to B_{ac}^{β}, an increase in losses of 6% is obtained just by increasing dv/dt from around 1 to 5 V/ns.

The noticeable difference in B–H loop for excitations with different dv/dt requires special attention from circuit designers, especially with the extreme switching speed of wide-bandgap devices. The switching speed in this test is low for what GaN devices can achieve, so the impact on real applications might be even more significant. Usually, B–H loop measurements are done with lower dv/dt. Similar figures where the impact of the transition is negligible with ZVS operation can be found in [33] and [53].

D. Impact of Duty Cycle in Triangular Waveforms

In this section, the effect of the duty cycle in triangular waveforms is illustrated in detail. Fig. 14 shows B–H loops with duty cycle from 0.2 to 0.8. The results are shown as a function of $D_P - D_N$. D_P is the duty cycle of the positive dB/dt period, and D_N is the duty cycle of the negative dB/dt period. The duty cycle affects dB/dt, impacting B–H loop area, and hence losses.

Fig. 15 illustrates how B–H loops change as f and B_{ac} change for a large duty cycle (80%). During the relatively long time when the current increases (D_P/f), the B–H loop section remains close to the quasi-static loop. In contrast, the loop area is heavily influenced by the short time where $B(t)$ is decreasing quickly (D_N/f). Fig. 15(b) shows how the impact of frequency is very significant in this rapidly changing region. Clearly, dB/dt largely determines the shape of the B–H loop. At
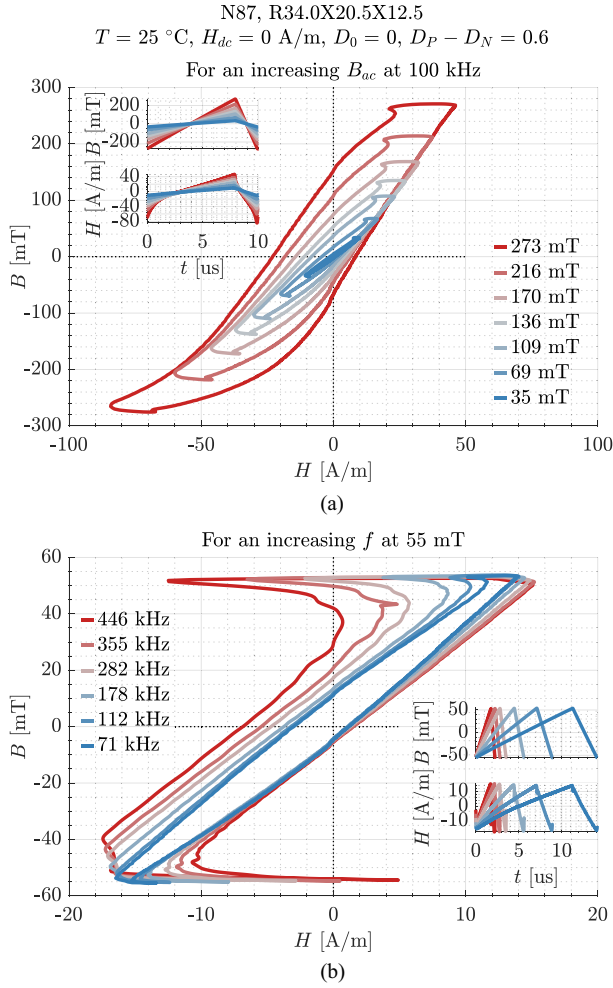
Fig. 15. Measured B–H loops for a triangular 80% duty cycle excitation at 25 °C without dc bias. (a) For different flux density amplitudes at 100 kHz. (b) For different frequencies at 55 mT. Compare it with Fig. 10.

Fig. 16. Effect of duty cycle on core losses for triangular excitations without dc bias at 25 °C at the B_{ac} and f for the waveforms in Fig. 14 and two more B_{ac} and f combinations with similar losses at 50% duty cycle.

high flux density, the current is distorted, and there is a significant difference between $|H_{max}|$ and $|H_{min}|$. Note that the impact of hard-switching transitions seems significant when the duty cycle and frequencies are high (see the curve at 446 kHz in Fig. 15(b), with a maximum dv/dt of around 5 V/ns), partly because a higher voltage is required for a given B_{ac}, which implies higher dv/dt, and partly because the peak and decay in H after the transition represent a larger fraction of the falling time.

Duty cycle heavily impacts core losses. Fig. 16 shows core losses obtained by interpolating the available data points as a function of duty cycle at 100 kHz and 55 mT (the same conditions used to plot the B–H loops in Fig. 14) and other excitations with similar losses at 50% duty cycle (i.e., 400 kHz, 25 mT, and 200 kHz, 40 mT). From a physics standpoint, quasi-static hysteresis is not impacted by waveform shape or frequency, but eddy currents are [12], [54].

Many models have been developed to capture the impact of waveform shapes on core losses. Reviews of state-of-the-art core loss models for other excitations can be found in [37], [53], and [55] and include models based on loss separation [41], [56] or
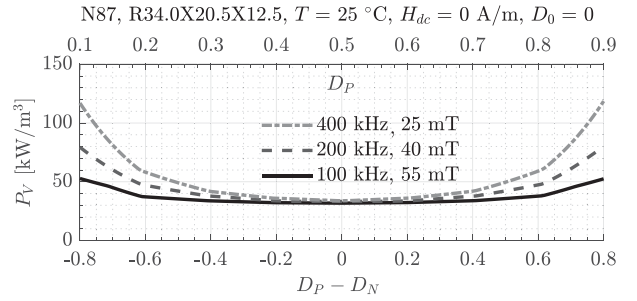
based on extending the Steinmetz equation to arbitrary waveforms. The latter include the modified Steinmetz equation [47], generalized Steinmetz equation [27], the improved generalized Steinmetz equation (iGSE) [57], and the improved improved generalized Steinmetz equation [37] among others. Further discussion on this topic is available in [29], [58], and [59]. For its simplicity, the iGSE remains the preferred method for core loss calculations. Yet all these methods rely on Steinmetz parameters, which are only accurate over limited frequency ranges and their choice can determine the accuracy [55], [60]. Methods that rely directly upon measured data have also been proposed. In [31], the composite waveform hypothesis—the assumption that the energy lost in each of the sections of a waveform can be added up—is introduced and applied to calculate losses in triangular waveforms of different duty cycles based solely on the core loss for 50% duty cycle triangular waveforms at different frequencies. This idea is better understood with an example: core losses for a triangular waveform with 2-μs rise time and 8-μs fall time (100 kHz switching frequency) are equal to half the losses of a 250-kHz 50% triangular waveform (2-μs rise time) plus half the losses of a 62.5-kHz 50% triangular waveform (8 μs rise time). A curve fit for this approximation is implemented in [55], and an extension to waveforms other than triangular is developed in [61].

The MagNet dataset can be used to evaluate the applicability and limitations of these methods. Fig. 17(a) shows the volumetric core loss for triangular waveforms with 80% duty cycle. The effect of duty cycle at different f and B_{ac} can be understood by comparing this figure with the data at 50% duty cycle in Fig. 11. The ratio between the losses at 80% and 50% duty cycle is shown in Fig. 17(b) to help compare the data. An important observation is that losses are not just increased by a constant factor depending on the duty cycle but rather are a function of f and B_{ac}, by a factor ranging from nearly 1 to 2 in this specific measurement range. This contradicts the results expected from iGSE if constant Steinmetz parameters are used. For triangular waveforms, P_V is proportional to $D_P^{1-\alpha} + D_N^{1-\alpha}$ for a given B_{ac} and f. These results highlight the need for α to depend on frequency at least.

The database can also be used to evaluate the composite waveform hypothesis [31]. To provide an example, the results from triangular waveforms at 70 and 400 kHz can be used to estimate the losses for waveforms with a 15.4% duty cycle
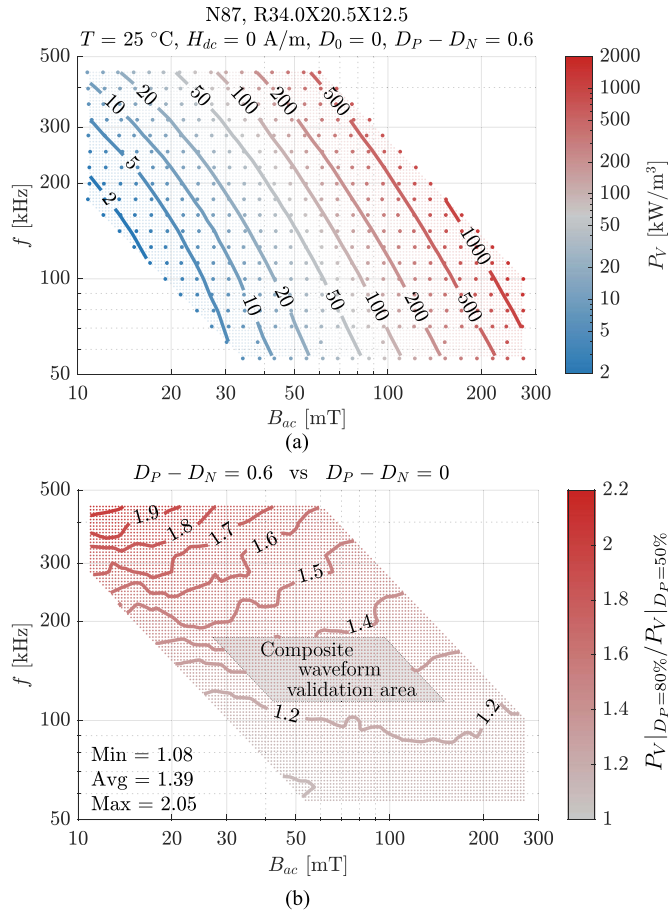
Fig. 17. Effect of duty cycle in volumetric core losses. (a) Core losses for triangular 80% duty cycle excitations without dc bias at 25 °C as a function of B_{ac} and f. (b) Ratio between P_V at 80% duty cycle and 50% duty cycle. The composite waveform hypothesis has been tested in the marked area.

Fig. 18. Core losses as a function of the duty cycle (in color) for a triangular duty cycle excitation at 25 °C and without dc bias. $D_P - D_N$ equal to 0 represents 50% duty cycle triangular waveform, while 1 represents a sawtooth waveform. (a) For increasing f for different $D_P - D_N$ values. (b) For increasing values of B_{ac} for a selection of $D_P - D_N$.

at 122 kHz. For 30 mT, the energy per cycle at 70 kHz is approximately 73.6 mJ/m³ and at 400 kHz it is 131.1 mJ/m³, while for 15.4% duty cycle and 122.3 kHz, the interpolated energy per cycle is 99.4 mJ/m³. The estimated energy per cycle based on the hypothesis is 102.4 mJ/m³, an excellent match (3% error) in this specific example. The same procedure can be applied to all data points in Fig. 17(b); the results, available only in the marked area, are underestimated by 2.4% on average, with a maximum discrepancy of 6.4% and a mean absolute error of 2.7%. This example shows that reasonable predictions of losses can be obtained based solely on 50% duty cycle data at this temperature and without dc bias.

The model proposed in [53] can also be evaluated using this database. In this model, core loss is described as the product of two independent factors: the static hysteresis loss, related to the amplitude and bias of the flux density, and another factor related to the waveform shape and frequency. Using the constants provided in [62] for the volumetric energy loss per cycle without dc bias and at 25 °C, the results for 80% duty cycle can be obtained. Losses are underestimated only by 5.3% on average when compared to the interpolated data in the range 50–300 mT and 50–400 kHz (from which the parameters are obtained). The maximum absolute error is 30% and the mean absolute error is

7.3% for this specific example. Since two different datasets are compared, this is not a direct comparison as different core sizes and core-to-core variation can also contribute to the reported error, which is discussed in Section III-H and Appendix F, respectively.

The effect of duty cycle on core loss can be better understood when plotted for different frequencies and flux densities as curves similar to the ones used in datasheets. Fig. 18 shows several of these curves. Duty cycles of 50%, 70%, 80%, 85%, and 90% are shown because changes in losses are more significant when the duty cycle is extreme [55]. The effect of duty cycle is far more severe at high frequencies, and, to a lesser extent, at low flux densities [see Fig. 18(a)], which helps to understand the comparison in Fig. 17(b). This high-frequency effect, partly because of the high frequency itself, and partly because of the large duty cycle, is no longer well captured by the Steinmetz equation since losses cannot be solely represented as a power law of frequency [see Fig. 18(b)]. Moreover, the core might start losing permeability at these frequencies.

N87, R34.0X20.5X12.5, $T = 25$ °C, $H_{dc} = 0$ A/m, $D_P - D_N = 0$
Increasing D_0 at 55 mT and 100 kHz
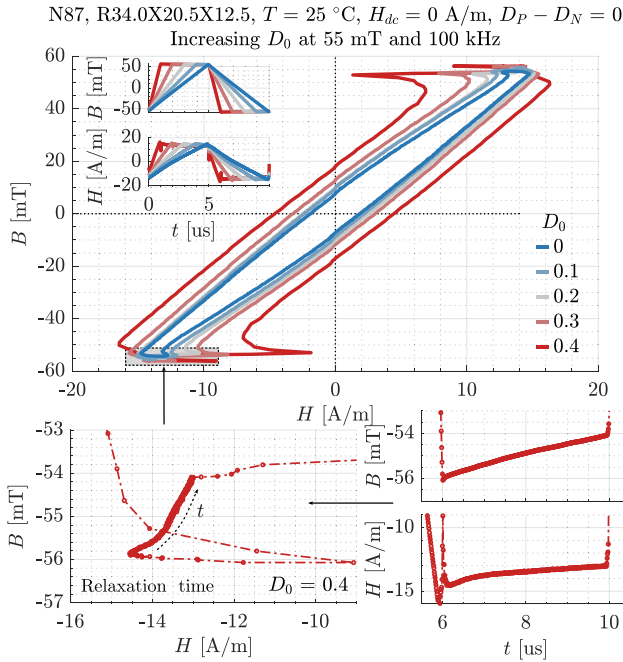

Fig. 19.   Measured $B-H$ loops for trapezoidal waveforms of different relaxation time and dB/dt at 25 °C, 100 kHz, and 55 mT without dc bias. A zoom of the negative $dB/dt \approx 0$ part for $D_0 = 0.4$ on the region where B and H are nearly constant is also included.

Waveform shape has only a mild effect on amplitude permeability in this magnetic material. The permeability decreases at all operating conditions when duty cycle is increased from 50% to 80%, in the f and B_{ac} range where measurements are available in both cases. A 4% average drop is found, with a maximum drop of 12% when the peak flux density is large. Since waveform shape does not considerably impact permeability, sinusoidal measurements might suffice for the characterization of this property.

E. Impact of Zero-Voltage Regions

MagNet includes data for trapezoidal B waveforms. To gain information on how zero-voltage regions ($dB/dt = 0$) impact the $B-H$ loop, measurements where the zero sequence represents different fractions of the total period can be plotted. Fig. 19 shows the measurements for a fixed frequency and flux density amplitude, where D_P equals D_N (same rise and fall time), and D_0 is changed (the duty cycle of the region where B is flat). A phenomenon called relaxation impacts the shape of $B-H$ loops. The relaxation phenomena can be observed during the zero sequences where H decays while B remains nearly constant, shown in the zoom of Fig. 19. It is also observed that the rate of change in H is not constant, but faster at the beginning of the relaxation time. The measurements show the same behavior reported in [37], although longer relaxation times are considered and the effect of switching transitions is negligible in that article. A description of relaxation processes can be found in [12]. Some models incorporate such effects (see [37] and [60] for example),
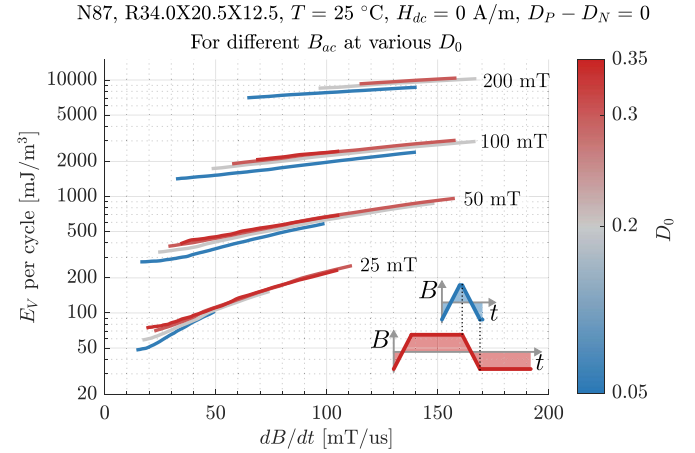
N87, R34.0X20.5X12.5, $T = 25$ °C, $H_{dc} = 0$ A/m, $D_P - D_N = 0$
For different B_{ac} at various D_0

Fig. 20.   Energy loss per cycle losses as a function of the duty cycle of the zero-voltage region, D_0, for trapezoidal symmetric excitation at 25 °C and without dc bias as a function of the dB/dt of the rising and falling parts of the trapezoidal waveform for given flux densities.

but other models such as iGSE do not. In this section, this impact is quantified.

The previous figure is not a direct study on the effect of relaxation time, as dB/dt during the rise and fall times is changing, and that is responsible for most of the change in the $B-H$ loop. Hence, core losses for different D_0 are not too useful. To study the effect of relaxation on losses, it is convenient to keep dB/dt constant while increasing the time the zero-voltage regions last. Fig. 20 is included to show the impact of the zero-voltage sequences by comparing volumetric losses per cycle and dB/dt for a few given B_{ac}, corresponding to waveforms where the frequency is not constant, but rather the dB/dt portions of the waveform are constant. It is concluded that the zero-voltage sequences negatively impact losses per cycle as expected from relaxation phenomena. Since the input voltage and current have similar levels for a given B_{ac} and dB/dt, the impact of dv/dt in the transitions described in Section III-C is expected to be independent of D_0 here.

Finally, the effect of sections of zero voltage is not significant in μ_a, ranging from -8% to $+4\%$, from the measurements where data are available at 20% rising and falling time with respect to 50% rising and falling time, showing that sinusoidal information can suffice for permeability calculations as mentioned before.

F. Effect of DC Bias

The dc bias level of the excitation, a variable that is not fully documented in datasheets, plays a critical role in power magnetics [63]. In this section, the effects of a dc bias in the current in the DUT are analyzed. As mentioned in Section II, H_{dc} is used for comparison, as B_{dc} cannot be inferred with the setup used. To visualize the impact of dc bias, Fig. 21 shows the measured "$(B - \overline{B})-H$" loops for 50% duty cycle triangular waveforms at an H_{dc} of 0, 15, 30, and 45 A/m. There is a clear change in permeability with the bias, which can be directly observed in $H(t)$. In addition, dc bias affects core losses considerably. Losses for the $B-H$ loops in Fig. 21 are included
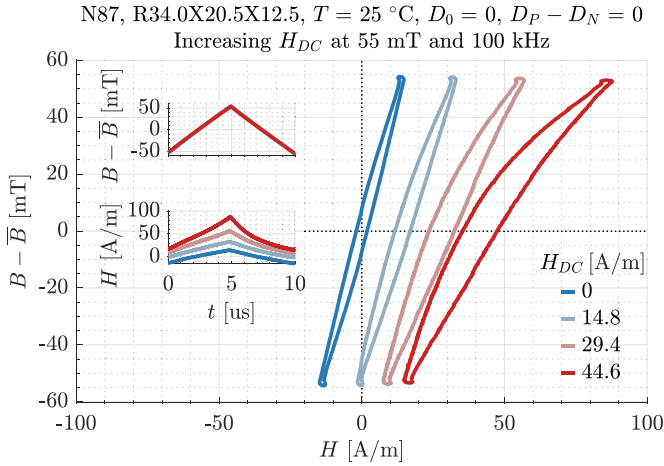
Fig. 21. Measured "$(B - \overline{B})$–H" loops for triangular 50% duty cycle waveforms at 25 °C, 100 kHz, and 55 mT for different dc bias. B_{dc} is not represented as it cannot be directly obtained from the measurements.
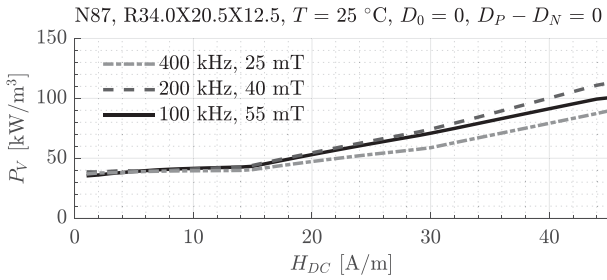

Fig. 22. Interpolated core losses as a function of H_{dc} for a few combinations of B_{ac} and f for 50% duty cycle triangular excitation at 25 °C. Instead of interpolating for H_{dc} directly, $\log_{10}|H_{dc}|$ is used as it provides more reasonable results. Note that data are measured in steps of 15 A/m.

Fig. 23. (a) Core losses for a triangular 50% duty cycle excitation at 25 °C and 45 A/m as a function of B_{ac} and f. (b) Ratio between losses in (a) and without dc bias (see Fig. 11). This ratio is referred to as the displacement factor in [67].

in Fig. 22. In this figure, a subset of the interpolated losses at different bias levels, frequencies, and flux density amplitudes for three combinations of B_{ac} and f is depicted. In this case, besides a logarithmic interpolation on B_{ac} and f, $\log_{10}|H_{dc}|$ is selected for interpolation across dc bias dimension rather than H_{dc} directly.

The literature on the impact of dc bias on core losses is extensive. Early measurements of the impact on dc bias in [63] and [64] report the highly nonlinear relation between bias and core losses. A review of the measuring options and effects of the dc bias on core losses is found in [65]. A more recent analysis, with data up to 3 MHz, can be found in [22]. Extensive measurements of the dc bias effect are also provided in [53]. In addition, a model is proposed where the dependence of losses with B_{ac} and B_{dc} is first extracted for quasi-static hysteresis and then modified by a factor that accounts for the frequency and shape of the excitation. An approach to account for this effect based on loss separation is introduced in [56]. The bias has been modeled in Steinmetz-based methods [47], [66], as well as accounted for by modifying the Steinmetz parameters for each H_{dc} [22], [67].

To dive more deeply into the impact of extreme H_{dc} on losses, Fig. 23(a) shows results for triangular waveforms with 50% duty
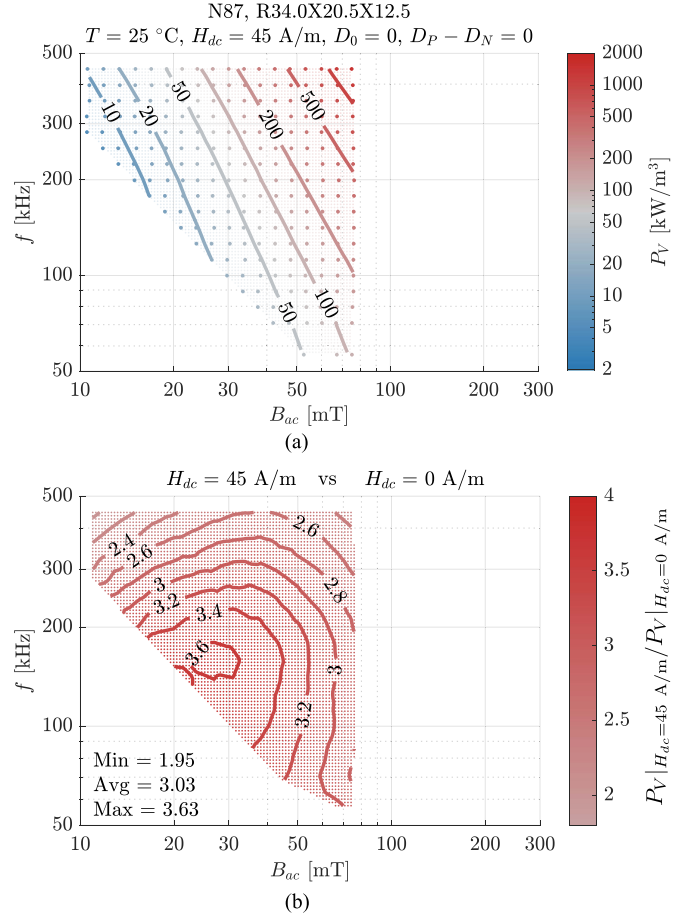
cycle at an H_{dc} of 45 A/m. To avoid saturation and excessive losses, tests at B_{ac} over 75 mT are not executed with this level of dc bias. To be able to draw meaningful conclusions, the ratio between the measurements at 45 and 0 A/m in the f–B_{ac} plane is shown in Fig. 23(b). On average, losses increase by a factor of 3 for this specific case, but the interesting feature is that this increment in losses is both frequency- and flux density dependent. The increase in losses with bias is less significant as higher frequencies, as discussed in [22]. Modeling these effects accurately is a pressing need for magnetic component designers. As discussed in [37], these measurements reveal the limitations of models, which decouple the dc bias effect from the frequency effect, such as [47] and [53], or models where the dc bias effect is assumed to be independent of the ac excitation, as in [64] (improved in [63]). The conclusion is that the impacts of frequency, flux density, and dc bias are coupled. More sophisticated modeling techniques are needed to obtain accurate predictions of core loss.

With a large dc bias, the amplitude permeability generally drops. For the 50% duty cycle triangular data at 25 °C and 45-A/m dc bias (about 250 mT if a relative permeability of 4400 is used to relate H_{dc} with B_{dc}), the relative amplitude permeability is around 1000, a substantial decrease compared

N87, R34.0X20.5X12.5, $H_{dc} = 0$ A/m, $D_0 = 0$, $D_P - D_N = 0$
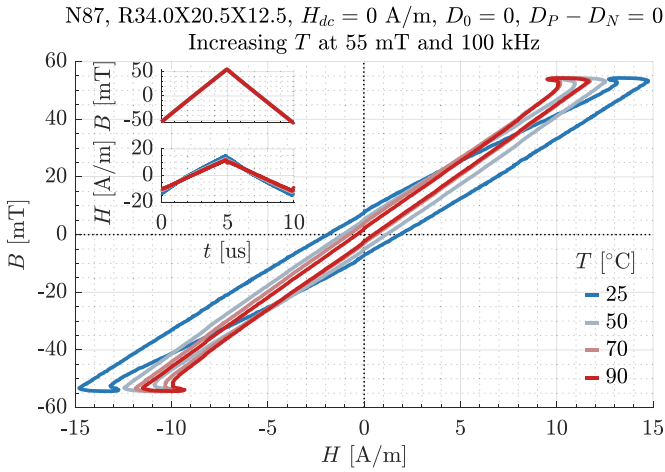Increasing T at 55 mT and 100 kHz

Fig. 24. Measured $B-H$ loops for a triangular 50% duty cycle excitation at without dc bias at 100 kHz and 55 mT for different temperatures.

with the results without dc bias in Fig. 12. It yields a ratio $\mu_a|_{H_{dc}=45\,\text{A/m}}/\mu_a|_{H_{dc}=0\,\text{A/m}}$ of 0.4 ± 0.03, changing slightly in different regions of the $f-B_{ac}$ plane. The effect is nearly constant across frequency and peak flux density, although the latter may be due to the small range of ac flux density tested (from 10 to 80 mT in this case).

G. Temperature Dependence

Core loss is also affected by external factors such as temperature because, among other reasons, permeability, permittivity, and conductivity are temperature dependent [9]. The $B-H$ characteristic is affected by temperature, as reported in datasheets for quasi-static conditions [see Fig. 1(a)]. For low frequencies, $B-H$ loop variations with temperature are studied in [68], and a model for the saturation with temperature is proposed in [26]. $B-H$ loops are shown in Fig. 24 for 25 °C, 50 °C, 70 °C, and 90 °C for 50% duty cycle triangular waveforms. In this temperature range, it can be observed how losses decrease with temperature, while amplitude permeability increases for this magnetic material, with changes being more significant at lower temperatures. N87 is a material with minimum losses and high permeability around 90–100 °C, highlighting that the material is designed for optimum performance at high temperatures. However, there are materials in the market to suit specific needs: reasonable temperature stability, losses nearly constant across wide temperature ranges, minimum losses at specific temperatures, and so on.

The datasheet information in Fig. 1(d) shows how temperature impacts core losses; however, for this specific material, the datasheet only provides data at 100 kHz. Although more data can be found in the manufacturer's software [11], data are only available for sinusoidal waveforms and without dc bias. In this article, triangular data are analyzed. Fig. 25 is included to show that core losses, although different in magnitude for sinusoidal and 50% duty cycle triangular waveforms, have similar overall trends with respect to temperature. In addition, this plot shows that having $P_V(T)$ for a single frequency can be misleading:

N87, R34.0X20.5X12.5, $H_{dc} = 0$ A/m
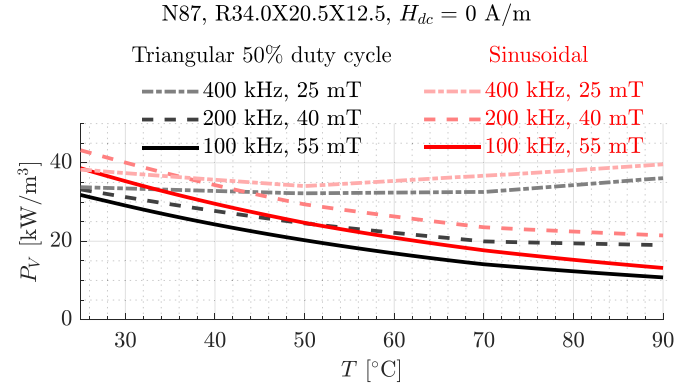
Fig. 25. Interpolated core losses as a function of T for a few B_{ac} and f conditions for sinusoidal and 50% duty cycle triangular excitations without dc bias.

N87, R34.0X20.5X12.5
$T = 90$ °C, $H_{dc} = 0$ A/m, $D_0 = 0$, $D_P - D_N = 0$

(a)

$T = 90$ °C   vs $T = 25$ °C

Min = 0.31
Avg = 0.64
Max = 1.42

(b)
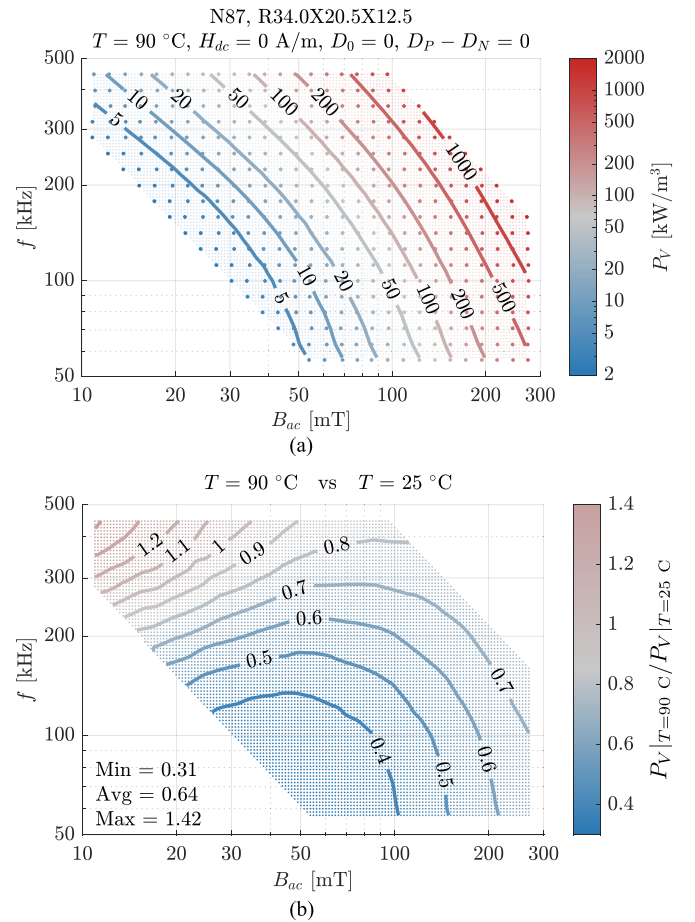
Fig. 26. (a) Core losses for a triangular 50% duty cycle excitation without dc bias at 90 °C as a function of B_{ac} and f, for comparison with the data in Fig. 11 at 25 °C. (b) Ratio between the volumetric core loss at 90 °C and 25 °C.

the trends for 100 and 400 kHz differ significantly. To clarify this effect, Fig. 26(a) shows the measured core losses at 90 °C for 50% duty cycle triangular waveforms, while Fig. 26(b) depicts the variation with respect to the results at 25 °C. At high frequencies and low flux densities, the behavior of core losses with respect to temperature reverses, and core losses

Fig. 27. Amplitude permeability for 50% duty cycle triangular excitations without dc bias as a function of temperature for a few B_{ac} and f combinations.

TABLE I
N87 CORES USED TO EVALUATE THE EFFECT OF CORE GEOMETRIES

TDK's denomination	h [mm]	$\frac{d_a - d_i}{2}$ [mm]	l_e [mm]	A_e [mm^2]	V_e [mm^3]	N
R58.3×40.8×17.6	17.6	**8.75**	152.4	152.4	23230	5
R34.0×20.5×12.5	12.5	**6.75**	82.06	82.60	6778	5
R25.3×14.8×10.0	10.0	**5.25**	60.07	51.26	3079	8
R16.0×9.6×6.3	6.30	**3.20**	38.52	19.73	760	14

Similar effects are observed on sinusoidal data although with a higher dependence on frequency.

Fig. 28. Ratio between the amplitude permeability at 90 °C and 25 °C for 50% duty cycle triangular excitations without dc bias, as a function of B_{ac} and f. The amplitude permeability at 25 °C is shown in Fig. 12.
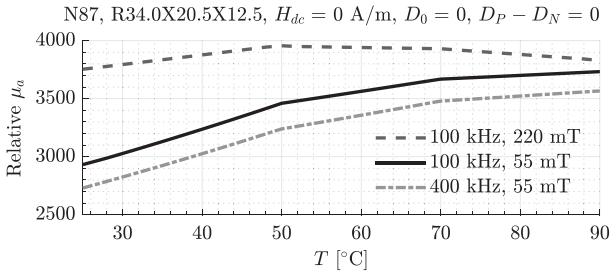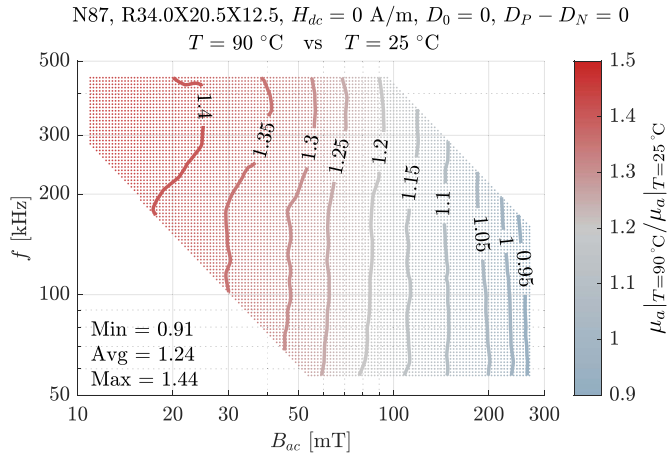
increase with temperature. From a physical standpoint, the area of the quasi-static B–H loop decreases with temperature [see Fig. 1(a)], leading to lower hysteresis loss, but the conductivity of N87 increases with temperature [14], leading to higher eddy currents and increasing losses. At high frequency and low flux density, this second effect could be dominant. In general, the effect of temperature is both frequency- and flux density dependent and has been typically addressed by providing different Steinmetz parameters at different temperatures or by modifying methods to add the temperature dependence [59].

Permeability is also affected by temperature, not only the initial permeability but also the amplitude permeability, as shown in Fig. 1(b). The data in MagNet can be used to plot amplitude permeability as a function of temperature rather than B_{ac}. The results for triangular data and different frequencies and flux densities are shown in Fig. 27. Note how for 220 mT, amplitude permeability is similar at 25 °C and 90 °C, which is coherent with the data provided in the datasheet [crossing between the curve at 25 °C and 100 °C in Fig. 1(b)]. Fig. 28 shows the ratio between the permeability at 90 °C and 25 °C for 50% duty cycle triangular waveform measurements. It agrees with μ_a reported in Fig. 1(b) even though triangular data are used instead of sinusoidal data. The plot shows how permeability increases with temperature, and the change is heavily influenced by peak flux density. Frequency has a slight impact at low flux density.

H. Core Size Impact

Core losses are not independent of core size and cannot be expressed by a constant volumetric loss only function of the magnetic material considered [69]. The magnitude of the magnetic field is not homogeneous inside the core. For instance, in toroids, the field is stronger in the inner radius than in the outer radius of the core. An analytical model for eddy currents accounting for field distribution can be found in [17], based on ferrite grain and grain boundary properties [18], [69], [70]. In addition, ferrites properties are not homogeneous for large cores because of firing/sintering processes [44], [50], [52]. Besides the variability in magnetic properties and the frequency-independent effect, skin effect and dimensional resonances also modify the magnetic field distribution in the core. These phenomena are related to the propagation of electromagnetic waves inside the core due to the high permeability and permittivity. They become significant at higher frequencies and depend on the dimensions of the core [8], [13], [14], [44], [50], [70], [71], [72]. A description of the physics behind these phenomena can be found in [12] and [52]. These effects are difficult to quantify because manufacturers do not provide adequate information on the electrical properties of the core [8], [54]. Models for the flux density distribution based on measurements of the electrical properties of the core are available in [13], but obtaining the distribution of H and B analytically can be complex. Finite-element simulations are effective tools for the calculation of such distributions [52]. The challenge, however, lies in the lack of accurate values for conductivity, permeability, and permittivity as a function of frequency and temperature [13], [70].

To study these effects, several different sizes of toroids have been measured under the same conditions employing the setup used to collect the data in MagNet to provide an estimate of the magnitude of the effect that core size has on magnetic properties. The onset of these frequency-dependent effects is dominated by the smaller of the two dimensions across the core area [13]. For toroids, this is either height h or external radius minus internal radius $(d_a - d_i)/2$. In this section, the results for 50% triangular waveforms at 25 °C without dc bias are discussed for the toroids listed in Table I. In all the cases, the smaller length is $(d_a - d_i)/2$, marked in the table.

Even though B and H depend on the position in the core, their "scalar values," calculated based on effective dimensions, are still a powerful way to understand and compare magnetics. B–H loops in similar B_{ac} conditions at 500 kHz, the highest frequency
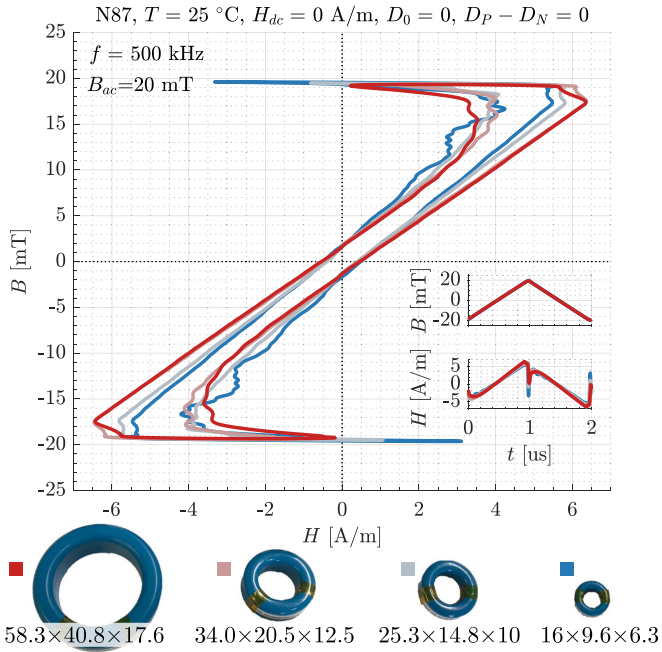
Fig. 29. Measured $B–H$ loops at 50% duty cycle 25 °C, 500 kHz, and nearly 20 mT without dc bias for different core geometries. Small differences in H_{dc} are removed to make the comparison easier.

tested, are shown in Fig. 29 for the core listed in Table I. Significant differences among the $B–H$ loops are observed that cannot be attributed to small changes in the excitation, dv/dt, or temperature changes. For instance, at this specific operation point, the volumetric loss in the large core is 32.4 kW/m^3, while the small core has only 26.3 kW/m^3. Relative amplitude permeability drops from 2800 in the small core to 2400 in the large core. However, these data must be read carefully, as tolerances in the core create variations on these numbers on the same order of magnitude, as reported in Appendix G.

Eddy current, skin effect, and dimensional resonances have different repercussions on core losses depending on the geometry, size, permeability, conductivity, and permittivity of the core [9], [18], [52]. Moreover, as discussed in [49], dielectric losses depend on core geometry and size. Yet, core losses are typically provided only for a given shape (R34.0 $\times$ 20.5 $\times$ 12.5 in the datasheet for N87 [10]). Measured losses for the four toroids as a function of f and B_{ac} are shown in Fig. 30. The variation, although small, is more significant than the expected error in the measurement (see the Appendix) showing that the size of the core impacts core losses. For instance, the ratio between the core loss of the large core with respect to the small core in the range where measurements are available in both cases is, on average, 1.16, with a maximum value of 1.31 at 500 kHz.

Similarly, amplitude permeability is also impacted. $\mu_a|_{\text{R58.3}\times40.8\times17.6}/\mu_a|_{\text{R16}\times9.6\times6.3}$ is 0.88 on average, almost equal at low frequency and high flux density but with a minimum of 0.85 at 500 kHz.

Considering the magnetic properties only to be a function of the material can be a misleading approach when deriving accurate models [15], [41]. This is problematic since the frequency/size at which this geometry-dependent phenomenon

Fig. 30. Core losses for different geometries of the N87 toroids for a triangular 50% duty cycle excitation without dc bias at 25 °C. (a) As a function of B_{ac} for a set of frequencies. (b) As a function of f for different values of B_{ac}.

starts is undetermined due to the lack of data [8]. Providing a frequency range for each material in datasheets is not enough, and the frequency range, core losses, and permeability should be specified for each combination of core and shape instead of being assumed as shape- and size-independent.

I. Material Impact

In this article, the properties of Mn–Zn soft ferrites are discussed using the material N87 as an example, but each material has its unique properties and, hence, distinct $B–H$ loops. Fig. 31 shows the core loss with 50% triangular excitations for several Mn–Zn ferrites from different manufacturers. One should read these plots carefully since the impact of geometry can skew the results favoring one material or another as they are not measured for the same dimensions. This graph also illustrates the relative importance that operating conditions (such as dc bias or geometry) can have over the selection of the proper material. It is beyond the scope of this article to investigate how the variation of magnetic properties is impacted by different parameters for all materials, but the data can be found in the MagNet database.
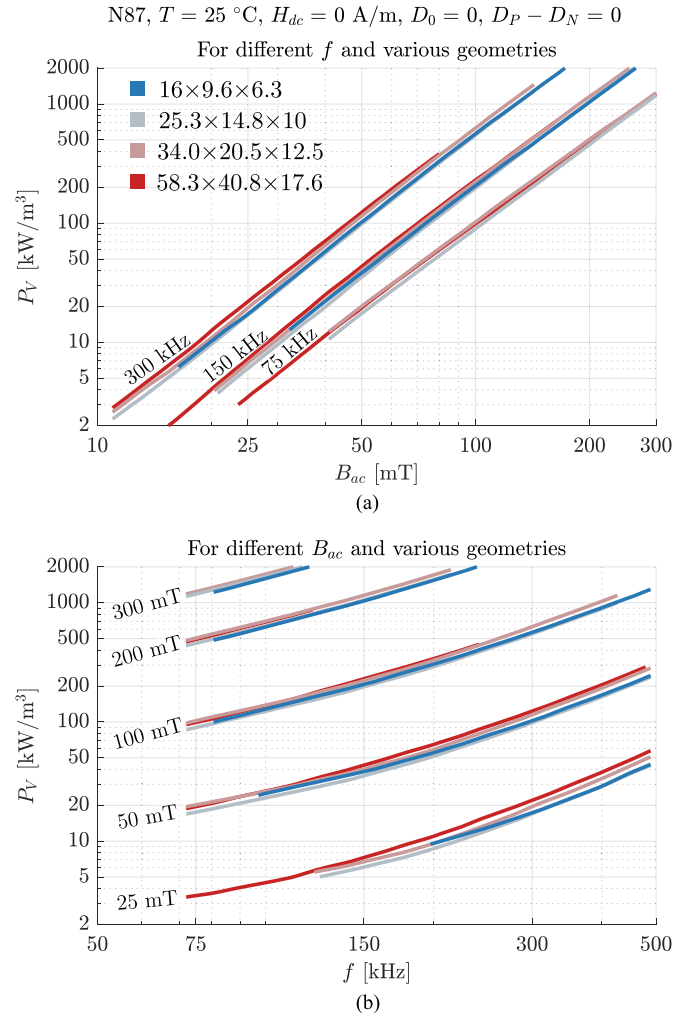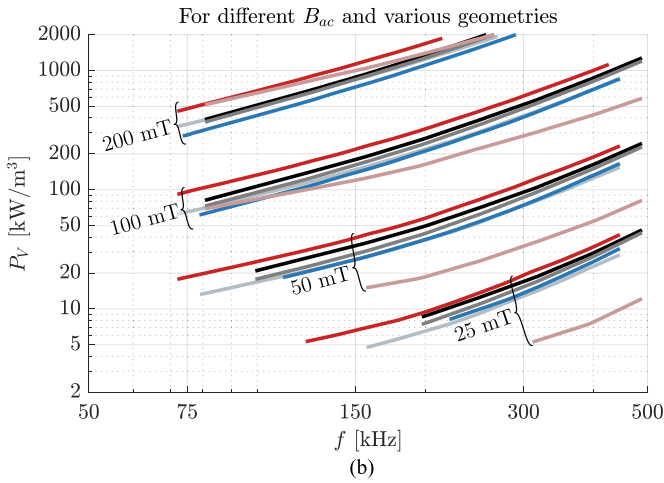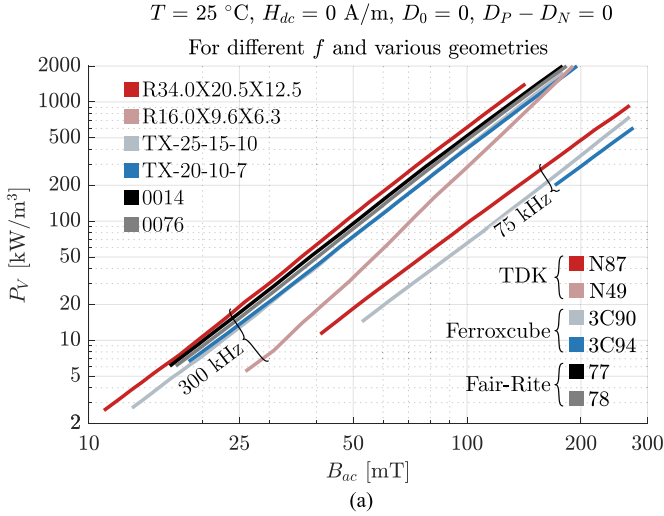
Fig. 31. Core losses for different Mn–Zn materials for a triangular 50% duty cycle excitation without dc bias at 25 °C. (a) As a function of B_{ac} for a set of frequencies. (b) As a function of f for different values of B_{ac}.

Fig. 32. Ratio between P_V at 80% duty cycle and 50% duty cycle at 90 °C. Compare with the data at 25 °C in Fig. 17(b).
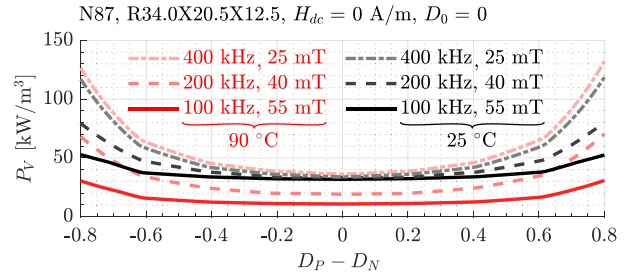
Fig. 33. Core loss for unbiased triangular waveforms against duty cycle for the set of curves in Fig. 16 for 25 °C together with the same curves for 90 °C.

IV. FEASIBILITY OF MODELS WITH DECOUPLED FACTORS

The goal of this section is to find whether different effects can be decoupled from one another based on the collected data. Since there is a relatively large variation from core to core (see Appendix G), only results for a single core are provided and the effect of geometry is not discussed. As noted in Section III-C, the effect of dv/dt cannot be eliminated and might distort this analysis. The small variations in temperature discussed in Appendix E cannot be discerned either. In addition, an important parameter affecting core loss not discussed in this article is the mechanical pressure applied to the core [9].

Traditionally, the effects of frequency and flux density have been modeled as independent of each other. For example, according to the Steinmetz equation, $P_V|_{B_{ac1}}/P_V|_{B_{ac2}}$ is a function of B_{ac1} and B_{ac2} but not of frequency (holding all other conditions constant). Similarly, from the Steinmetz equation, $P_V|_{f_1}/P_V|_{f_2}$ is related by the factor α, which might depend on f slightly but should not depend on B_{ac}. This is valid to a large extent; for instance, in Fig. 7(b), the ratio $P_V|_{B_{ac1}}/P_V|_{B_{ac2}}$ (which is the slope of $P_V(B_{ac})$) does not considerably change
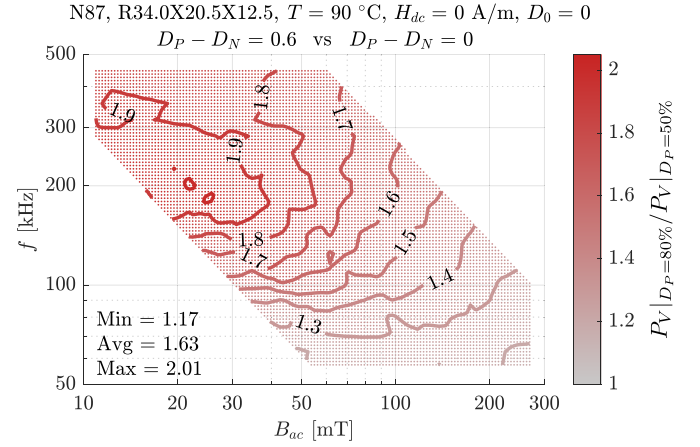
for different frequencies. Similarly, from Fig. 7(c), the slope of the $P_V(f)$ curves is similar for different flux densities (although the slope changes with frequency).

It is important to know to which extent, the effects on losses of other parameters (temperature, dc bias, or duty cycle) are independent of one another. Equations in the form of $P_V(B_{ac}, f, H_{dc}, D, T) = k \cdot f(B_{ac}) \cdot f(f) \cdot f(H_{dc}) \cdot f(D) \cdot f(T)$, or similar, where each contribution adds a multiplicative factor are unlikely valid. To check which factors can be linked to and decoupled from others, the ratio between power losses under different conditions is examined. For instance, Fig. 32 shows the variation of losses from 50% to 80% duty cycle at 90 °C. In this case, $P_V|_{D_1}/P_V|_{D_2}$ clearly depends on the frequency or peak flux density considered. Furthermore, we can see an additional layer of complexity by comparing Fig. 32 to Fig. 17(b), which shows the same ratio, but for 25 °C. $P_V|_{D_1}/P_V|_{D_2}$ is slightly temperature dependent (the ratio is different in both plots). A clearer picture of the combined effect of temperature and duty cycle is included in Fig. 33 for three sets of frequencies and flux densities. Although, at first sight, the temperature seems to create a relatively constant shift in the losses regardless of duty cycle when looking closely at the curves at 200 kHz and 40 mT, the difference in losses between 90 °C and 25 °C decreases significantly at extreme duty cycles.

Similarly, the effects of temperature and dc bias are heavily coupled. In [63], the increase of losses because of dc bias is found

Fig. 34.   Ratio between P_V at 45 A/m and 0 A/m dc bias at 90 °C. Compare with the data at 25 °C in Fig. 23(b).

Fig. 36.   Ratio between P_V at 80% and 50% duty cycle at 45 A/m. The range is limited to the frequencies and flux densities where data are available for both duty cycles. Compare with the data at 0 A/m in Fig. 17(b).

Fig. 35.   Core loss against dc bias for triangular 50% duty cycle waveforms at 25 °C and 90 °C. for a few combinations of B_{ac} and f. The same interpolation used in Fig. 22 is selected.
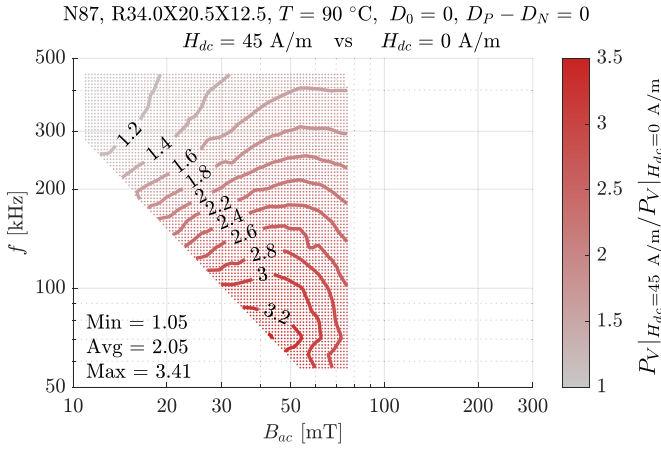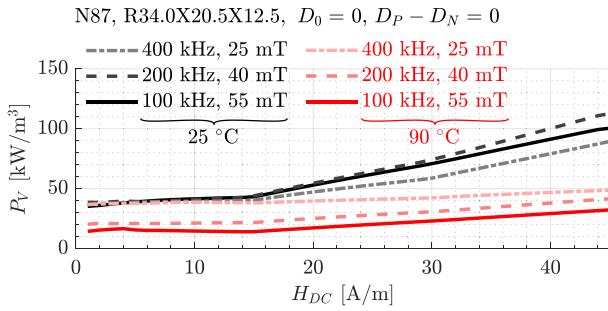

Fig. 37.   Core loss for triangular data at 25 °C for the curves in Fig. 16 without bias together with the same curves for 45 A/m. Extrapolated data are removed to avoid artifacts.

to be frequency and geometry dependent at low flux densities. Fig. 34 shows the ratio of P_V at 45 A/m dc and 0 A/m at 90 °C. Compare this figure to Fig. 23(b), which depicts the same ratio at 25 °C. Not only in value (for instance, the average increase in losses at 25 °C is 200% while at 90 °C is 100%) but trends are heavily affected. Therefore, the effect of H_{dc} on losses is significantly influenced by f and B_{ac}. For a better understanding, Fig. 35 shows how core losses increase with dc bias for a few triangular waveforms under different conditions. Temperature significantly attenuates the impact of dc bias as just mentioned.

The coupled effect of duty cycle and dc bias can also be observed by comparing $P_V|_{D_P=80\%}/P_V|_{D_P=50\%}$ at 45 A/m in Fig. 36 with the results at 0 A/m in Fig. 17(b). Again, although the relation with respect to B_{ac} and f is similar, the maximum variation at 0 A/m is 2.05, while the maximum variation at 45 A/m is only 1.67. Interestingly, dc bias gives rise to an asymmetrical duty cycle impact on losses. To give an example, for dc biased data with 45 A/m measured at $\sim$75 mT and $\sim$56 kHz, losses are 121 kW/m^3 for 80% duty cycle but 142 kW/m^3 for 20% duty cycle. For a fuller picture, see Fig. 37, where losses are plotted against duty cycle at 0 and 45 A/m. These relations cannot be accounted for by models treating the effect of dc bias to be independent of the effect of waveform shape for given frequencies, peak flux densities, and temperatures.

From the measurements, $P_V(B_{ac}, f, H_{dc}, D, T)$ cannot be decoupled into any set of multiplicative factors dependent on different parameters if high accuracy across a wide range of operating conditions is desired. Note that measurements are subject to errors and the temperature stability should be further improved as detailed in the Appendix, but it is unlikely for measurement errors to give rise to flawed overall trends. This analysis does not advise against loss separation models where different loss contributions are added up, and each contribution is a function of a few parameters (for instance, the static hysteresis contribution is independent of waveform shape or frequency), but decoupling these effects while accounting for the impact of geometry might not valid either, as discussed in [52]. Instead, this work advises against unified models where any additional variable (bias for instance) acts as a factor modifying the total losses. Eventually, to obtain satisfactory models for any waveform shape, losses should be defined as $P_V(t) = f(B(t), T)$. From this time-dependent equation, special cases (steady state operation or triangular waveforms without bias as examples) could be derived and then described as a function of desired

parameters (e.g., frequency and duty cycle). A further step would be to have models where the uneven distribution of $B(t)$ in different parts of the core is accounted for, hence having models depending on the geometry of the core.

Intricate empirical models could be proposed as a solution, but complex models are hardly going to be adopted by designers and are likely to be difficult or unstable to parameterize. Empirical solutions parameterized with subsets of data can be a reasonable framework, but extrapolation to other operating conditions should be avoided. In general, models capturing the impact of individual factors may provide useful guidelines to the design process, but may not accurately describe the material behaviors when many factors co-exist. Extensive datasets to create loss maps and direct interpolation might also be applied. Unfortunately, the available measurements from manufacturers do not cover all the realistic operation scenarios. Better physics-based models are likely to improve the accuracy of the predictions and point other models in the right direction, but usually, pushing research forward needs experiments where some of the effects can be safely neglected. Integrating models that account for different phenomena can be complex in the end, bringing us again to the intricate and hard-to-use models. Finally, machine learning techniques, such as neural networks, can be employed to model core loss accounting for all the desired parameters, yet again, accurate and extensive datasets are needed for training [15]. Neural networks in this framework can be considered as a form of efficient interpolation of the data, where the information is stored in the structured weights and biases of the network rather than data points [21]. Challenges with machine learning models include compatibility and integration with existing tools and difficulties with generalizations to scenarios different from the test dataset.

V. CONCLUSION

In this article, the data in MagNet have been employed to explain and quantify the challenges power magnetics modeling has to overcome. Extensive $B–H$ loop, core loss, and permeability data have been analyzed to illustrate how peak flux density, frequency, waveform shape, dc bias, temperature, core size, and core material impact the behavior of the magnetic core. This analysis supports the results of other researchers where each of these factors or a few factors are studied in detail but brings an additional challenge: studying each parameter affecting the core $B–H$ loop independently is not the best approach to follow, as these effects are intertwined. For this reason, it is difficult to make a simple yet accurate model for magnetic materials valid in a wide range of operating conditions. Machine learning models, such as neural networks, can capture the effect of the different parameters with reasonable accuracy if a reliable dataset covering the range of operating conditions and waveforms that are of interest is available for training. We hope this article motivates other researchers to develop new models and share their measurements, aiming to have a large open-source database covering operating regions where data lack accuracy or are not currently available in the MagNet database.

APPENDIX DETAILED ERROR ANALYSIS

Understanding the sources of error is a necessary step to ensure the accuracy and validity of the $B–H$ measurements [32]. In this appendix, the procedure to obtain the different errors in the setup and their sources are described. Similar discussions can be found in [32], [67], and [73] for their respective setups using the $V–I$ method. All the problems have been tackled to the extent possible, yet the data are not error-free. Besides the errors reported here, data processing can introduce additional errors. These errors strongly depend on the accuracy of the frequency detection algorithm. Note that since errors are heavily influenced by test conditions, a single number to provide accuracy is not representative of the complete dataset. In this section, the error is shown for the measurements of the N87 material with 50% triangular waveforms at 25 °C without dc bias, but similar error maps can be created for each operating condition and material in the MagNet database.

A. Effect of Phase Delay

A known problem of the two-winding method is the effect of phase mismatch between the voltage and current measurements. Since reactive power is much larger than average power, a small phase shift can cause a large error in loss estimation. This error is regarded as the main limitation of this method when it comes to high-frequency measurements [30], [32], [34], [65], [74]. Since the parasitic capacitance and inductance in the shunt are not expected to be a problem in the considered frequency range [32] and the delay between two channels in the oscilloscope is negligible (≤ 100 ps), the most significant source of error in this setup credits the different delays caused by the unmatched length of the probes. A delay of 1.6 ns has been measured (0.3° at 500 kHz for reference) by comparing the current measurement with the voltage probe when measuring the same current. This delay is not compensated. Other sources of delay are listed in [32].

The effect of delays in the measurements for sinusoidal waveforms is explained as an additional phase shift because of the delay on top of the phase shift caused by the restive behavior of losses [74]. For simplicity, the worst case absolute error is analyzed here. This is the case for a lossless inductor. The discrepancy in power for a sinusoidal voltage of amplitude V and sinusoidal current of amplitude I shifted and t_{delay} with respect to the ideal 90° and simplified using the small-angle approximation is given by

$$\Delta P_{\text{max}} \approx V \cdot I \cdot |t_{\text{delay}}| \cdot \pi \cdot f. \quad (6)$$

This simple equation relates the frequency, reactive power $S = V \cdot I/2$, and time delay with the error in losses. ΔP_{max} increases with frequency and results in large relative errors for materials/operation points where the quality factor is high.

This approximation can be used to obtain the worst case variation in losses for PWM waveforms as well. In essence, the delay in current causes a discrepancy in the average current in each one of the switching states. This variation in current multiplied by the applied voltage gives rise to active power. As
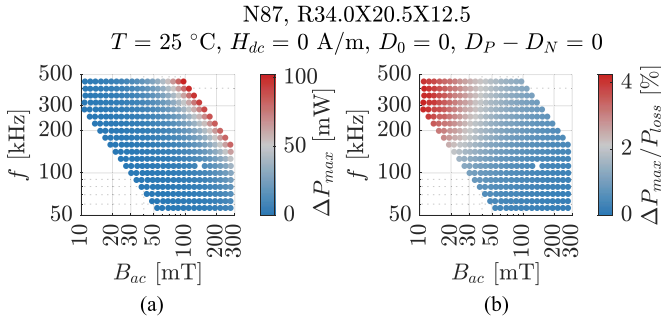
Fig. 38. Effect of 1.6-ns delay between the voltage and current measurement on a subset of the N87 data. (a) Worst case added or subtracted losses. (b) Relative error.

Fig. 39. Scale for the voltage and current used for the tests for triangular 50% duty cycle waveforms at 25 °C without dc bias measurements.

long as $t_{\text{delay}} \ll d \cdot T$, on a first approximation, for trapezoidal symmetric and triangular waveforms of any duty cycle, this variation in measured loss is given by

$$\Delta P_{\max} \approx V_{\text{in}} \cdot I_{\text{pk}} \cdot |t_{\text{delay}}| \cdot 4 \cdot f. \tag{7}$$

As an example, the error due to a delay of 1.6 ns can be estimated for triangular 50% duty cycle waveforms at 25 °C without dc bias (the data shown in Fig. 11) by considering the measured voltages and currents waveforms as those of a lossless inductor and using (7). This worst case error in the measured losses is shown in Fig. 38(a). Even though the error in losses is significantly higher with increasing f and B_{ac}, so do the measured losses. As a result, the relative error depends not only on frequency but also on the quality factor of the operation point, as shown in Fig. 38(b). The relative error due to the phase shift is below 5% for N87, but a higher relative error would be obtained for low-loss materials and higher frequencies (24% in the worst operation point for N49 for the 50% triangular data in MagNet for instance). Deskewing is strongly recommended if the two-winding method is used for frequencies in the MHz range.

B. Effect of Probes and Oscilloscope Error

The probes and oscilloscope add up errors because of changes in gain, offset, and vertical resolution. These errors depend on the vertical scale used to capture the data. The voltage and current vertical scales are [0.5, 1, 2, 5, 10, 20, 50] V and [0.01, 0.02, 0.05, 0.1, 0.2, 0.5, 1] V, respectively (current is measured using a 0.964-Ω equivalent resistance). A 40% margin is left between the maximum value of the signal and the maximum value the oscilloscope can read to avoid clipping. The vertical scales used for the measurements for the subset of data are shown in Fig. 39 to clarify the oscilloscope setup.

The gain error between samples is specified as a constant part, the dc gain accuracy, which is $\pm 1.5\%$ for the Tektronix DPO4054, a constant 1.2-mV error, and a variable part, which is 0.15 times the volts per division. Therefore, larger vertical scales imply higher absolute error. This equation and values are used to calculate peak-to-peak error in the oscilloscope based on the technical reference [75] and considered a basis for this analysis, although real errors are not so large since this is probably the absolute maximum error provided by the
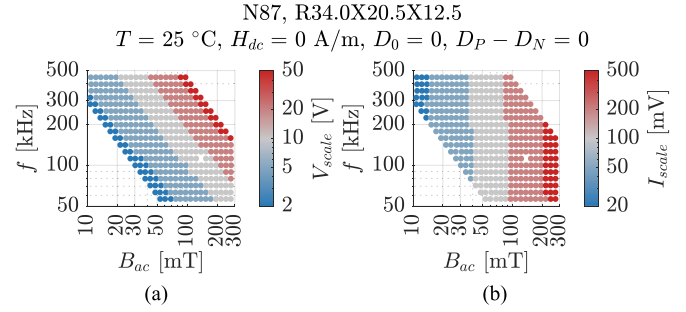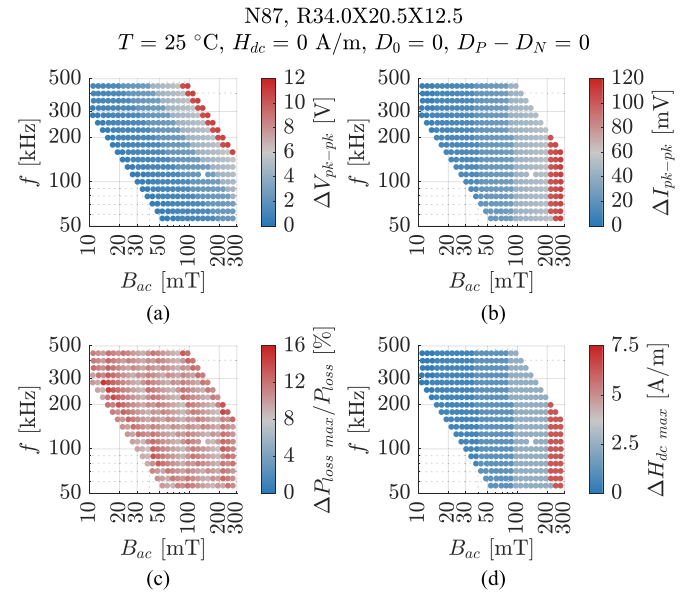

Fig. 40. Effect of the gain and offset errors in the measurements of N87 triangular 50% waveforms at 25 °C without dc bias. (a) Worst case error because of the passive probe and scope in the peak-to-peak voltage measurement. (b) Worst case error because of the passive probe and scope in the peak-to-peak current measurement. (c) Worst case relative error in the core loss; calculated as $(V_{\text{pk-pk}} + \Delta V_{\text{pk-pk}}) \cdot (I_{\text{pk-pk}} + \Delta I_{\text{pk-pk}})/(V_{\text{pk-pk}} \cdot I_{\text{pk-pk}}) - 1$. (d) Worst case absolute error in dc bias due to offset.

manufacturer. Moreover, the passive probe P6139A has $\pm 0.5\%$ attenuation, and the accuracy of the shunt resistor (T&M Research W-5-10-1STUD) is $\pm 0.2\%$. The total worst case relative error added by the scope and probes is shown in Fig. 40(a)–(c), in the voltage measurement, the current measurement, and the loss calculation, respectively. A fixed 3.7% error is the result of the dc gain accuracy and probes errors and tolerances. The constant 1.2-mV factor mostly deteriorates data at low currents (up to 1%). Most of the error is related to the vertical scale selected, up to 5% because of the voltage near the change of vertical scale region from 2 to 5 V or from 20 to 50 V and other 5% near the change from 20 to 50 mV and from 200 to 500 mV for the current measurement. The error distribution follows a pattern mostly dictated by the changes in the vertical scale. Note that this is the worst case error, the distribution of the error is unknown, and it is very unlikely that all the errors add up in both voltage and current

Fig. 41. B–H loops for one of the measured waveforms with the values of amplitude permeability and core loss calculated from the B and H signals. (a) Measured B–H loop. (b) Downsampling the number of points per cycle from 1024 to 64 and rounding V and I to one-tent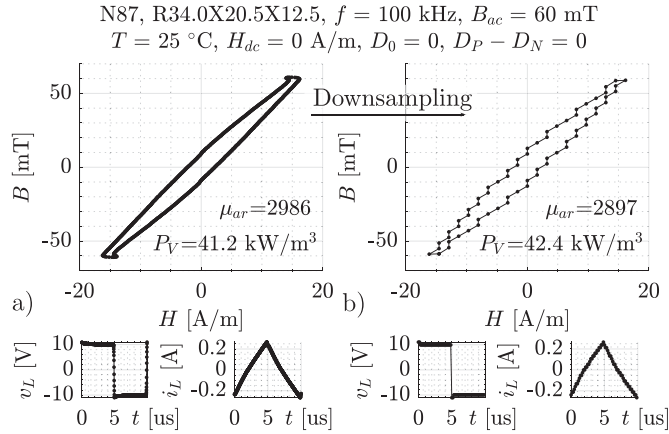h of their respective peak-to-peak values. The effect on losses and permeability is not so significant even in such an extreme case.

measurements at the same time as in the plot. The expected error is discussed in Appendix F. A better oscilloscope could lead to more accurate results. A limitation of the dc bias measurement is that the scale for the current remains large even for low I_{ac} due to the large I_{dc}, leading to lower accuracy at larger dc bias. Also, note that the error on the voltage measurement directly affects the reported B_{ac}.

Regarding the offset error, since the average voltage is removed from the measurement during data processing, it does not pose a problem. However, the offset in the current measurement affects H_{dc}. The offset error is 0.2 of the selected vertical scale. The error, in absolute terms, is shown in Fig. 40(d) for the current scale shown in Fig. 39(b), translated to H for convenience. The maximum error reaches about 6 A/m.

The random noise is not expected to affect measurements, and it is mostly removed by the 20-MHz filter in the oscilloscope. The error of this filter is considered negligible as the fundamental frequency of the excitations is limited to 500 kHz. Tests without the filter show negligible variation in core loss.

The last concern when using an oscilloscope to collect data is the effect of the vertical and horizontal resolution. The number of bits for the vertical resolution (8 bits with this scope) and the number of samples (800 ps sampling time and averaging every ten samples) can limit the accuracy of the B–H loop. Fortunately, the effects on permeability or loss calculation are not significant. For illustration, Fig. 41 shows one of the measured loops subjected to additional heavy downsampling. P_V or μ_a is not too affected even in such extreme conditions, although results can change from point to point. In general, the measurements are not affected much by sampling effects at this level. B is less prone to error compared to H as it results from the integration of the voltage. Moreover, the single-cycle algorithm considerably reduces the effects of downsampling, both in the horizontal and vertical scales. Since the average of several switching cycles is used, the resulting waveform is averaged out. As a result, the resolution is not expected to cause a significant error in these measurements.

C. Effect of Parasitic Elements in the Circuit

There are several parasitic elements affecting the measurements [22], [34]. Since a secondary winding is used for voltage measurements, the effect of winding resistance and leakage inductance (both in primary and secondary) can be safely neglected. The input resistance of the passive probe is large enough (10 MΩ) so its current can be neglected. However, any capacitive element in parallel with the DUT can impair the current measurement. This includes the parasitic capacitance of the primary winding, the capacitance of the secondary winding, the parasitic capacitance of the passive probe (8.0 pF) (which is reflected in primary), and any additional capacitance from the leads connecting the device to the shunt. Note that the capacitance of the winding is larger when submerged in oil as compared to air. The critical problem is that winding capacitance is largely influenced by the core if windings are wound close to the core, even if turns are sufficiently far apart from one another [51]. As such, the core gives rise to a capacitive and resistive behavior, as briefly studied in Section III-C. By increasing the distance to the core by means of thicker insulation for the wire, bobbins, or the use of coated cores, this capacitance can be minimized. Unfortunately, in this article, Litz wire is used, so the distance from the conductors to the core is minimal. Even if the coupling between the windings and core capacitance is minimized, the core presents capacitive behaviors, which should not be considered an error but part of the magnetic material properties.

When a sinusoidal voltage is applied, the current through this parasitic capacitance is nearly 180° shifted with respect to the DUT current, and, as a result, the measured current has a lower amplitude than the real value. As a reference, for 500 kHz and 70 μH, a ∼70 pF in parallel with the DUT would cause a 5% variation in the current measurement. For PWM waveforms, the effect is a large current through the capacitor during the dv/dt region. Then, the measured current in the shunt shows a dip during the transition depending on the transition speed, which is not caused by the behavior of the core solely, as discussed in Section III-C.

The second source of error is the parasitic elements in the current measurement circuit. Any inductance or capacitance in the shunt resistor would change the measured voltage. Nevertheless, these effects can be disregarded as the bandpass frequency of the selected shunt is 800 MHz. The parasitic capacitance of the BNC connector for the shunt is lower than 10 pF. Besides the capacitance of the shunt itself, the primary-to-secondary capacitance of the DUT has a similar effect as it is grounded in secondary through the passive probe. This capacitance phase shifts the current measurement. For the DUT, a 25-pF primary-to-secondary capacitance is measured when submerged in oil. Considering a 1-Ω shunt measuring a sinusoidal current at 500 kHz, this capacitance creates an additional 0.044° phase shift, negligible compared to the 0.3° phase shift because of the probes.

D. Nonideal Excitations

Any changes in the voltage or current measurement from one cycle to the next can cause additional errors. This error is evaluated during the data processing stage, and rogue data are removed. Then, note that waveforms are not as ideal as listed. Sinusoidal waveforms can be slightly distorted (and total harmonic distortion (THD) is calculated as a measure to address its quality), and triangular and trapezoidal waveforms do not have perfect edges. Hard switching (or partial or incomplete ZVS) leads to different current waveforms during the transition depending on the frequency and voltage of the excitation. For instance, for 10% duty cycle at 500 kHz, the dead time (70 ns) is comparable with D_P/f (200 ns). In addition, the control times can only be set as an integer number of clock cycles, so exact frequencies and duty cycles are not always attainable. Finally, the shunt and parasitic resistances make the impedance of the load not purely inductive, creating a voltage drop that can distort the voltage excitation. Note that this is not a problem for the calculations but rather for how data are reported, because $B(t)$ and $H(t)$ are directly obtained from the measurements. The error is introduced when parameterizing $B(t)$ waveforms in terms of waveform shape (duty cycles).

E. Effect of the Variation in Temperature During Testing

Due to the average losses during the continuous swapping of operation points, the temperature in the core may rise even with the core submerged in an oil tank at a controlled temperature (see Section II-A). This small temperature change can have a subsequent impact on losses. For instance, the temperature of the core right after a set of tests for triangular 25 °C no dc bias measurements for all frequencies and flux densities, which takes about 15 min, was 30 °C (using a thermal camera). This 5 °C variation in reported temperature has an impact on losses. Moreover, at 90 °C water temperature, the oil temperature is slightly lower (87 °C), also affecting the quality of the data. The temperature profile of the core during testing is not known as the core is submerged in oil. A complete analysis of the maximum variation between the set temperature and the external temperature of the core is yet to be done, and further improvements, such as adding a waiting time between tests or measuring the core temperature, could help mitigate this issue.

F. Assessing Reproducibility

One of the main drawbacks of inferring B from v_L is that the initial magnetization of the core is unknown. The voltage is only captured after the core has been excited for a short amount of time once steady-state operation has been reached (~0.5 s). This is a fundamental limitation and can be challenging as the history of $B(t)$ impacts the subsequent B waveform. Fortunately, accommodation reduces the impact of the magnetic history with the number of switching cycles [33], [76]. Moreover, a demagnetization sequence is briefly applied after the test at the highest B_{ac} for each frequency. Therefore, it is reasonable to expect similar results in the measurements regardless of the initial B_0 before the excitation is applied.
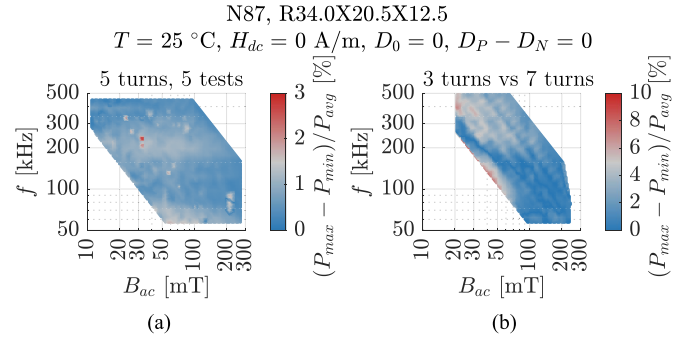

Fig. 42. Reproducibility of the measurements evaluated by the maximum relative variation in losses given by $(P_{\max} - P_{\min})/P_{\mathrm{avg}}$ of the interpolated results for the same core. (a) Five sets of tests. (b) For a different number of turns in the regions where data are available for both.

To validate the reproducibility of the measurement, the set of tests at 25 °C without dc bias for 50% duty cycle triangular waveforms has been repeated five times using the same DUT. Core losses can be evaluated to determine the impact that statistical errors have on the system. Fig. 42(a) shows the variation between the maximum and minimum core losses measured out of the five tests. On average, the error is 0.75% spread randomly across the f–B_{ac} plane. The same analysis, but in terms of amplitude permeability, gives a maximum variation between the five tests below 0.72% on average. As a result, it is concluded that statistical errors in the setup can be safely ignored. Note that the same testing sequence is used for the five cases, as such errors because of magnetic history or other systematic errors cannot be assessed.

Similarly, to evaluate how parasitics or the selection of the vertical scale in the oscilloscope affect the quality of the data, the same core has been tested using a different number of turns, as suggested in [32]. Instead of five turns, seven and three turns have been wound, and the relative variation in core loss between the two tests is shown in Fig. 42(b). Up to an 8% difference is measured, although the average is only 2.1%. This value, although not negligible, is acceptable as it is lower than the variation from core to core discussed in the following section.

G. Effect of the Variation of the Core Parameters

B and H are estimated based on A_e and l_e using (2) and (3), and volumetric losses are reported based on V_e using (4). In this article, the effective parameters listed in the datasheet are used. The tolerances of the effective parameters are calculated based on the tolerances on the diameter and height provided for uncoated toroids since the authors could not find any better source for this tolerance. For instance, for the R34.0 $\times$ 20.5 $\times$ 12.5 toroid, the inner diameter d_i is specified as 20.5 ± 0.5 mm, the outer diameter d_o is 34.0 ± 0.7 mm, and the height h is 12.5 ± 0.3 mm. The effective parameters, from the IEC-60205 standard [77], are given by

$$l_e = \frac{\pi \ln \frac{d_o}{d_i}}{\frac{1}{d_i} - \frac{1}{d_o}}, \quad A_e = \frac{h}{2} \frac{\ln^2 \frac{d_o}{d_i}}{\frac{1}{d_i} - \frac{1}{d_o}}, \quad V_e = \frac{h}{2} \frac{\pi \ln^3 \frac{d_o}{d_i}}{\left(\frac{1}{d_i} - \frac{1}{d_o}\right)^2}. \quad (8)$$
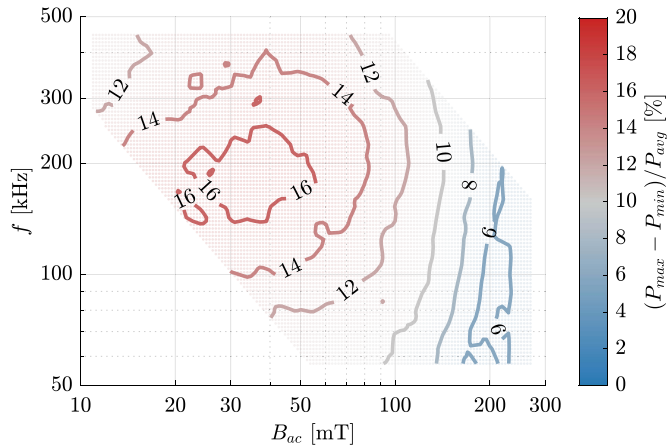
Fig. 43. Contour of the maximum relative variation in losses of the interpolated results for the different R34.0 × 20.5 × 12.5 N87 cores tested with triangular 50% duty cycle excitation at 25 °C without dc bias.

The minimum, nominal, and maximum effective lengths are 80.2, 82.06, and 83.92 mm, respectively, which represent a $\pm 2.3\%$ tolerance. This error is reflected in the reported H. For the effective area, the values are 73.72, 82.6, and 91.74 mm^2 for minimum, nominal, and maximum, respectively. The impact can be very significant, leading to $+10.75\%$, -11.06% in A_e, implying a $\sim \pm 11\%$ maximum error in the reported $B(t)$. Finally, the effective volume, nominally 6778 mm^3, can be as low as 6070 mm^3 and as high as 7497 mm^3; $+10.4\%$ and -10.6%. This effect implies a maximum error in the reported volumetric loss of about 10% too. This error is probably overestimated, but data on the tolerance of effective parameters are not readily available. Note that to lower this error, manufacturers would have to provide narrower definitions for the specified distances of the core, or the dimensions of DUTs should be carefully measured. Finally, not only dimensions but also material properties might change from core to core because of slightly different conditions during the manufacturing process. For instance, a tolerance of $\pm 25\%$ for the initial permeability for N87 material is reported in the datasheet, and a variation of 100% in conductivity between two cores is found in [14].

Both the change in effective parameters and core properties affect the behavior of cores. To check the impact of these effects (independent of the measurement system), five equal cores bought from the same distributor have been measured, all of them using the same winding configuration listed in Section II-A. The results are depicted in terms of maximum relative variation between tests in Fig. 43, showing a maximum variation of 16% from one core to another, but this variation is not constant in the $f-B_{\rm ac}$ plane. Interestingly, none of the five cores consistently has the highest or lowest core loss, but a core can have higher losses than the other only in certain parts of the $f-B_{\rm ac}$ plane. The same analysis could be performed with the relative amplitude permeability. On average, the maximum discrepancy between the five tests is 7.4%, 10.6% peak, which is within the tolerance specified by the manufacturer for initial permeability. The variation is spread more evenly than for losses,

so a plot is not needed. This variation in parameters gives an idea of the accuracy that models and measurements should target and are only worth improving if lower material tolerances are achievable.

REFERENCES

[1] C. O. Mathúna, N. Wang, S. Kulkarni, and S. Roy, "Review of integrated magnetics for power supply on chip (PwrSoC)," *IEEE Trans. Power Electron.*, vol. 27, no. 11, pp. 4799–4816, Nov. 2012.

[2] C. R. Sullivan, B. A. Reese, A. L. F. Stein, and P. A. Kyaw, "On size and magnetics: Why small efficient power inductors are rare," in *Proc. Int. Symp. 3D Power Electron. Integr. Manuf.*, 2016, pp. 1–23.

[3] M. Sankarasubramanian et al., "Magnetic inductor arrays for Intel fully integrated voltage regulator (FIVR) on 10th generation Intel core$^{\rm TM}$ SoCs," in *Proc. IEEE 70th Electron. Compon. Technol. Conf.*, 2020, pp. 399–404.

[4] C. R. Sullivan and M. Chen, "Coupled inductors for fast-response high-density power delivery: Discrete and integrated," in *Proc. IEEE Custom Integr. Circuits Conf.*, 2021, pp. 1–8.

[5] C. Sullivan, "Optimal choice for number of strands in a Litz-wire transformer winding," *IEEE Trans. Power Electron.*, vol. 14, no. 2, pp. 283–291, Mar. 1999.

[6] M. Chen, M. Araghchini, K. K. Afridi, J. H. Lang, C. R. Sullivan, and D. J. Perreault, "A systematic approach to modeling impedances and current distribution in planar magnetics," *IEEE Trans. Power Electron.*, vol. 31, no. 1, pp. 560–580, Jan. 2016.

[7] C. Sullivan, "Computationally efficient winding loss calculation with multiple windings, arbitrary waveforms, and two-dimensional or three-dimensional field geometry," *IEEE Trans. Power Electron.*, vol. 16, no. 1, pp. 142–150, Jan. 2001.

[8] G. Skutt and F. Lee, "Characterization of dimensional effects in ferrite-core magnetic devices," in *Proc. 27th Annu. IEEE Power Electron. Spec. Conf.*, 1996, vol. 2, pp. 1435–1440.

[9] M. Kacki, M. S. Ryłko, J. G. Hayes, and C. R. Sullivan, "Measurement methods for high-frequency characterizations of permeability, permittivity, and core loss of Mn-Zn ferrite cores," *IEEE Trans. Power Electron.*, vol. 37, no. 12, pp. 15152–15162, Dec. 2022.

[10] Ferrites and accessories—N87 material. Accessed: Jun. 2023. [Online]. Available: https://www.tdk-electronics.tdk.com

[11] TDK electronics: Ferrite magnetic design tool ver.5.6.1. Accessed: Jun. 2023. [Online]. Available: https://www.tdk-electronics.tdk.com/en/180490/design-support/design-tools/ferrite-magnetic-design-tool

[12] J. Goodenough, "Summary of losses in magnetic materials," *IEEE Trans. Magn.*, vol. 38, no. 5, pp. 3398–3408, Sep. 2002.

[13] M. Kacki, M. S. Ryłko, J. G. Hayes, and C. R. Sullivan, "Analysis and experimental investigation of high-frequency magnetic flux distribution in Mn-Zn ferrite cores," *IEEE Trans. Power Electron.*, vol. 38, no. 1, pp. 703–716, Jan. 2023.

[14] T. P. Todorova, A. Van den Bossche, and V. C. Valchev, "A procedure for the extraction of intrinsic ac conductivity and dielectric constant of N87 Mn-Zn ferrite samples based on impedance measurements and equivalent electrical circuit modeling," *IEEE Trans. Power Electron.*, vol. 33, no. 12, pp. 10723–10735, Dec. 2018.

[15] N. Rasekh, J. Wang, and X. Yuan, "Artificial neural network aided loss maps for inductors and transformers," *IEEE Open J. Power Electron.*, vol. 3, pp. 886–898, 2022.

[16] H. Zhao, C. Ragusa, C. Appino, O. de la Barrière, Y. Wang, and F. Fiorillo, "Energy losses in soft magnetic materials under symmetric and asymmetric induction waveforms," *IEEE Trans. Power Electron.*, vol. 34, no. 3, pp. 2655–2665, Mar. 2019.

[17] H. P. Rimal, G. Stornelli, A. Faba, and E. Cardelli, "Macromagnetic approach to the modeling in time domain of magnetic losses of ring cores of soft ferrites in power electronics," *IEEE Trans. Power Electron.*, vol. 38, no. 3, pp. 3559–3568, Mar. 2023.

[18] F. Fiorillo, C. Beatrice, O. Bottauscio, and E. Carmi, "Eddy-current losses in Mn-Zn ferrites," *IEEE Trans. Magn.*, vol. 50, no. 1, Jan. 2014, Art. no. 6300109.

[19] H. Li, D. Serrano, S. Wang, T. Guillod, M. Luo, and M. Chen, "Predicting the B-H loops of power magnetics with transformer-based encoder-projector-decoder neural network architecture," in *Proc. IEEE Appl. Power Electron. Conf. Expo.*, 2023, pp. 1543–1550.

[20] H. Li et al., "How MagNet: Machine learning framework for modeling power magnetic material characteristics," techRxiv, Preprint, 2022. [Online]. Available: https://doi.org/10.36227/techrxiv.21340998.v3

[21] M. Chen, H. Li, D. Serrano, and S. Wang, "MagNet-AI: Neural network as datasheet for magnetics modeling and material recommendation," techRxiv, Preprint, 2023. [Online]. Available: https://doi.org/10.36227/techrxiv.22726115.v1

[22] B. N. Sanusi, M. Zambach, C. Frandsen, M. Beleggia, A. M. Jørgensen, and Z. Ouyang, "Investigation and modeling of DC bias impact on core losses at high frequency," *IEEE Trans. Power Electron.*, vol. 38, no. 6, pp. 7444–7458, Jun. 2023.

[23] T. Guillod, P. Papamanolis, and J. W. Kolar, "Artificial neural network (ANN) based fast and accurate inductor modeling and design," *IEEE Open J. Power Electron.*, vol. 1, pp. 284–299, 2020.

[24] "Princeton-dartmouth-Plexim MagNet project: Data-driven methods for power magnetics modeling," Accessed: Jul. 8, 2023. [Online]. Available: https://mag-net.princeton.edu/

[25] H. Li et al., "MagNet: An open-source database for data-driven magnetic core loss modeling," in *Proc. IEEE Appl. Power Electron. Conf. Expo.*, 2022, pp. 588–595.

[26] H. Y. Lu, J. G. Zhu, and S. Y. R. Hui, "Measurement and modeling of thermal effects on magnetic hysteresis of soft ferrites," *IEEE Trans. Magn.*, vol. 43, no. 11, pp. 3952–3960, Nov. 2007.

[27] J. Li, T. Abdallah, and C. Sullivan, "Improved calculation of core loss with nonsinusoidal waveforms," in *Proc. IEEE Ind. Appl. Soc. Annu. Meeting*, 2001, vol. 4, pp. 2203–2210.

[28] E. Stenglein, D. Kuebrich, M. Albach, and T. Duerbaum, "Novel fit formula for the calculation of hysteresis losses including dc-premagnetization," in *Proc. Int. Exhib. Conf. Power Electron., Intell. Motion, Renewable Energy Energy Manage.*, 2019, pp. 1–8.

[29] P. C. Sarker, M. R. Islam, Y. Guo, J. Zhu, and H. Y. Lu, "State-of-the-art technologies for development of high frequency transformers with advanced magnetic materials," *IEEE Trans. Appl. Supercond.*, vol. 29, no. 2, Mar. 2019, Art. no. 7000111.

[30] Y. Han and Y.-F. Liu, "A practical transformer core loss measurement scheme for high-frequency power converter," *IEEE Trans. Ind. Electron.*, vol. 55, no. 2, pp. 941–948, Feb. 2008.

[31] C. R. Sullivan, J. H. Harris, and E. Herbert, "Core loss predictions for general PWM waveforms from a simplified set of measured data," in *Proc. 25th Annu. IEEE Appl. Power Electron. Conf. Expo.*, 2010, pp. 1048–1055.

[32] V. Thottuvelil, T. Wilson, and H. Owen, "High-frequency measurement techniques for magnetic cores," *IEEE Trans. Power Electron.*, vol. 5, no. 1, pp. 41–53, Jan. 1990.

[33] E. Stenglein, B. Kohlhepp, D. Kübrich, M. Albach, and T. Dürbaum, "GaN-half-bridge for core loss measurements under rectangular ac voltage and dc bias of the magnetic flux density," *IEEE Trans. Instrum. Meas.*, vol. 69, no. 9, pp. 6312–6321, Sep. 2020.

[34] E. Stenglein, D. Kuebrich, M. Albach, and T. Dürbaum, "Guideline for hysteresis curve measurements with arbitrary excitation: Pitfalls to avoid and practices to follow," in *Proc. Int. Exhib. Conf. Power Electron., Intell. Motion, Renewable Energy Energy Manage.*, 2018, pp. 1–8.

[35] S. Wang et al., "A simplified dc-bias injection method with mirror transformer for magnetic material characterization," in *Proc. IEEE Appl. Power Electron. Conf. Expo.*, 2023, pp. 1565–1571.

[36] P. Welch, "The use of fast Fourier transform for the estimation of power spectra: A method based on time averaging over short, modified periodograms," *IEEE Trans. Audio Electroacoust.*, vol. AU-15, no. 2, pp. 70–73, Jun. 1967.

[37] J. Mühlethaler, J. Biela, J. W. Kolar, and A. Ecklebe, "Improved core-loss calculation for magnetic components employed in power electronic systems," *IEEE Trans. Power Electron.*, vol. 27, no. 2, pp. 964–973, Feb. 2012.

[38] F. Preisach, "On the magnetic aftereffect," *IEEE Trans. Magn.*, vol. 53, no. 3, Mar. 2017, Art. no. 0700111.

[39] D. Jiles and D. Atherton, "Theory of ferromagnetic hysteresis," *J. Magnetism Magn. Mater.*, vol. 61, pp. 48–60, 1986.

[40] F. Liorzou, B. Phelps, and D. Atherton, "Macroscopic models of magnetization," *IEEE Trans. Magn.*, vol. 36, no. 2, pp. 418–428, Mar. 2000.

[41] W. Roshen, "Ferrite core loss for power magnetic components design," *IEEE Trans. Magn.*, vol. 27, no. 6, pp. 4407–4415, Nov. 1991.

[42] A. Laudani, G. M. Lozito, and F. R. Fulginei, "Dynamic hysteresis modelling of magnetic materials by using a neural network approach," in *Proc. AEIT Annu. Conf. Res. Ind., Need More Effective Technol. Transfer*, 2014, pp. 1–6.

[43] M. Tian, H. Li, and H. Zhang, "Neural network model for magnetization characteristics of ferromagnetic materials," *IEEE Access*, vol. 9, pp. 71236–71243, 2021.

[44] E. C. Snelling, *Soft Ferrites, Properties and Applications*. Cambridge, U.K.: Iliffe, 1969.

[45] W. G. Hurley, T. Merkin, and M. Duffy, "The performance factor for magnetic materials revisited: The effect of core losses on the selection of core size in transformers," *IEEE Power Electron. Mag.*, vol. 5, no. 3, pp. 26–34, Sep. 2018.

[46] G. Bertotti, "General properties of power losses in soft ferromagnetic materials," *IEEE Trans. Magn.*, vol. 24, no. 1, pp. 621–630, Jan. 1988.

[47] J. Reinert, A. Brockmeyer, and R. De Doncker, "Calculation of losses in ferro- and ferrimagnetic materials based on the modified Steinmetz equation," *IEEE Trans. Ind. Appl.*, vol. 37, no. 4, pp. 1055–1061, Jul./Aug. 2001.

[48] M. Luo, D. Dujic, and J. Allmeling, "Modeling frequency-dependent core loss of ferrite materials using permeance-capacitance analogy for system-level circuit simulations," *IEEE Trans. Power Electron.*, vol. 34, no. 4, pp. 3658–3676, Apr. 2019.

[49] M. Baumann, C. Drexler, J. Pfeiffer, J. Schueltzke, E. Lorenz, and M. Schmidhuber, "Investigation of core-loss mechanisms in large-scale ferrite cores for high-frequency applications," in *Proc. 24th Eur. Conf. Power Electron. Appl.*, 2022, pp. 1–10.

[50] W. Fano, S. Jacobo, and A. Razzitte, "Effect of sintering conditions on resistivity and dielectric properties of Mn-Zn ferrites," in *Proc. Annu. Rep. Conf. Elect. Insul. Dielectr. Phenomena*, 1999, vol. 1, pp. 297–300.

[51] L. Dalessandro, F. da Silveira Cavalcante, and J. W. Kolar, "Self-capacitance of high-voltage transformers," *IEEE Trans. Power Electron.*, vol. 22, no. 5, pp. 2081–2092, Sep. 2007.

[52] T. Dimier and J. Biela, "Non-linear material model of ferrite to calculate core losses with full frequency and excitation scaling," *IEEE Trans. Magn.*, vol. 59, no. 7, Jul. 2023, Art. no. 6300610.

[53] E. Stenglein and T. Dürbaum, "Core loss model for arbitrary excitations with DC bias covering a wide frequency range," *IEEE Trans. Magn.*, vol. 57, no. 6, Jun. 2021, Art. no. 6302110.

[54] S. Yamada, E. Otsuki, and T. Otsuka, "AC resistivity of Mn-Zn ferrites," in *Proc. 13th Int. Telecommun. Energy Conf.*, 1991, pp. 703–708.

[55] S. Barg, K. Ammous, H. Mejbri, and A. Ammous, "An improved empirical formulation for magnetic core losses estimation under nonsinusoidal induction," *IEEE Trans. Power Electron.*, vol. 32, no. 3, pp. 2146–2154, Mar. 2017.

[56] Z. Yan, Z. Weibo, and T. Guanghui, "A core loss calculation method for DC/DC power converters based on sinusoidal losses," *IEEE Trans. Power Electron.*, vol. 38, no. 1, pp. 692–702, Jan. 2023.

[57] K. Venkatachalam, C. Sullivan, T. Abdallah, and H. Tacca, "Accurate prediction of ferrite core loss with nonsinusoidal waveforms using only Steinmetz parameters," in *Proc. IEEE Workshop Comput. Power Electron.*, 2002, pp. 36–41.

[58] D. Rodriguez-Sotelo, M. A. Rodriguez-Licea, I. Araujo-Vargas, J. Prado-Olivarez, A. I. Barranco-Gutiérrez, and F. J. Perez-Pinal, "Power losses models for magnetic cores: A review," *Micromachines (Basel)*, vol. 13, 2022, Art. no. 418.

[59] J. Y. Alsawalhi and S. D. Sudhoff, "Saturable thermally-representative Steinmetz-based loss models," *IEEE Trans. Magn.*, vol. 49, no. 11, pp. 5438–5445, Nov. 2013.

[60] S. Barg and K. Bertilsson, "Core loss calculation of symmetric trapezoidal magnetic flux density waveform," *IEEE Open J. Power Electron.*, vol. 2, pp. 627–635, 2021.

[61] T. Guillod, J. S. Lee, H. Li, S. Wang, M. Chen, and C. R. Sullivan, "Calculation of ferrite core losses with arbitrary waveforms using the composite waveform hypothesis," in *Proc. IEEE Appl. Power Electron. Conf. Expo.*, 2023, pp. 1586–1593.

[62] E. Stenglein, "Messtechnische charakterisierung und vorhersage der kernverluste bei weichmagnetischen ferriten," Ph.D. dissertation, Dept. Electromagnetic Fields, Friedrich-Alexander-Universität, Erlangen, Germany, 2021.

[63] A. Brockmeyer and J. Paulus-Neues, "Frequency dependence of the ferrite-loss increase caused by premagnetization," in *Proc. Appl. Power Electron. Conf.*, 1997, vol. 1, pp. 375–380.

[64] A. Brockmeyer, "Experimental evaluation of the influence of DC-premagnetization on the properties of power electronic ferrites," in *Proc. Appl. Power Electron. Conf.*, 1996, vol. 1, pp. 454–460.

[65] C. A. Baguley, B. Carsten, and U. K. Madawala, "The effect of dc bias conditions on ferrite core losses," *IEEE Trans. Magn.*, vol. 44, no. 2, pp. 246–252, Feb. 2008.

[66] W. K. Mo, D. Cheng, and Y. Lee, "Simple approximations of the dc flux influence on the core loss power electronic ferrites and their use in design of magnetic components," *IEEE Trans. Ind. Electron.*, vol. 44, no. 6, pp. 788–799, Dec. 1997.

[67] J. Mühlethaler, J. Biela, J. W. Kolar, and A. Ecklebe, "Core losses under dc bias condition based on Steinmetz parameters," in *Proc. Int. Power Electron. Conf.*, 2010, pp. 2430–2437.

[68] M. Yang et al., "Magnetic properties measurement and analysis of high frequency core materials considering temperature effect," *IEEE Trans. Appl. Supercond.*, vol. 30, no. 4, Jun. 2020, Art. no. 5900905.

[69] Y. Sakaki and T. Matsuoka, "Hysteresis losses in Mn-Zn ferrite cores," *IEEE Trans. Magn.*, vol. 22, no. 5, pp. 623–625, Sep. 1986.

[70] K. Shimizu et al., "Loss simulation by finite-element magnetic field analysis considering dielectric effect and magnetic hysteresis in EI-shaped Mn-Zn ferrite core," *IEEE Trans. Magn.*, vol. 54, no. 11, Nov. 2018, Art. no. 7402705.

[71] W. Grimmond, A. Moses, and P. Ling, "Geometrical factors affecting magnetic properties of wound toroidal cores," *IEEE Trans. Magn.*, vol. 25, no. 3, pp. 2686–2693, May 1989.

[72] K. Namjoshi, J. Lavers, and P. Biringer, "Eddy-current power loss in toroidal cores with rectangular cross section," *IEEE Trans. Magn.*, vol. 34, no. 3, pp. 636–641, May 1998.

[73] M. Luo, D. Dujic, and J. Allmeling, "Modeling frequency independent hysteresis effects of ferrite core materials using permeance-capacitance analogy for system-level circuit simulations," *IEEE Trans. Power Electron.*, vol. 33, no. 12, pp. 10055–10070, Dec. 2018.

[74] M. Mu, Q. Li, D. J. Gilham, F. C. Lee, and K. D. T. Ngo, "New core loss measurement method for high-frequency magnetic materials," *IEEE Trans. Power Electron.*, vol. 29, no. 8, pp. 4374–4381, Aug. 2014.

[75] *MSO4000 and DPO4000 Series Digital Phosphor Oscilloscopes— Specifications and Performance Verification*, Tektronix, Beaverton, OR, USA. Accessed: Oct. 2022. [Online]. Available: https://download.tek.com/manual/077024701Rev_A_web.pdf

[76] E. Stenglein, D. Kübrich, M. Albach, and T. Dürbaum, "Influence of magnetic history and accommodation on hysteresis loss for arbitrary core excitations," in *Proc. 21st Eur. Conf. Power Electron. Appl.*, 2019, pp. P.1–P.10.

[77] *Calculation of the Effective Parameters of Magnetic Piece Parts*, IEC Standard 60205, 2006.

Shukai Wang (Graduate Student Member, IEEE) received the B.S. degree in electrical engineering from Michigan State University, East Lansing, MI, USA, in 2021, and the M.A. degree in electrical engineering in 2023 from Princeton University, Princeton, NJ, USA, where he is currently working toward the Ph.D. degree.

His research interests include magnetic modeling and related topics, and high-frequency wireless power transfer applications.
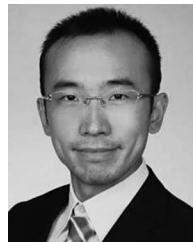
Mr. Wang was the recipient of the Outstanding Presentation Award at 2023 IEEE Applied Power Electronics Conference and Exposition.

Thomas Guillod (Member, IEEE) received the M.Sc. and Ph.D. degrees in electrical engineering from the Swiss Federal Institute of Technology (ETH) Zürich, Zürich, Switzerland, in 2013 and 2018, respectively, with focus on power electronics, numerical analysis, and field theory.

He was a Postdoctoral Researcher with the Power Electronic Systems Laboratory, ETH Zürich. Then, he was an Independent Engineering Consultant for both the industrial and academic projects. In 2021, he joined the Thayer School of Engineering, Dartmouth College, Hanover, NH, USA, as a Research Associate. His current research interests include high-frequency magnetic components, high-frequency power magnetic materials, and advanced numerical modeling techniques.

Diego Serrano received the B.S. degree in industrial electronic engineering from the Universidad de Granada, Granada, Spain, in 2015, and the master's degree in electronic engineering and the Ph.D. degree in power electronics from the Universidad Politécnica de Madrid (UPM), Madrid, Spain, in 2016 and 2021, respectively.

He was a Researcher with Centro de Electrónica Industrial, UPM, where he worked for another year as a Researcher. He is currently a Postdoctoral Research Associate with Princeton University, Princeton, NJ, USA, where he is working on the measurement and modeling of magnetic materials. His research interests include multilevel conversion, applications with gallium nitride and silicon carbide devices, and magnetics.

Min Luo (Senior Member, IEEE) received the B.S. degree in electrical engineering from Tsinghua University, Beijing, in 2009, the M.S. degree in electrical power engineering from RWTH Aachen University, Aachen, Germany, in 2012, and the Ph.D. degree in electrical engineering from the Swiss Federal Institute of Technology Lausanne (EPFL), Lausanne, Switzerland, in 2018.

From 2012 to 2022, he was with Plexim GmbH, Zürich, Switzerland, working on modeling and hardware-in-the-loop test systems for power electronics. From 2020 to 2023, he was responsible for electronic design of unmanned aerial vehicle propulsion systems with Ekarus Engines GmbH, Essingen, Germany. He is currently a Marketing Representative with BASiC Semi, Zürich.

Haoran Li (Graduate Student Member, IEEE) received the B.S. degree in electrical engineering from Tsinghua University, Beijing, China, in 2019, and the M.A. degree in electrical and computer engineering in 2021 from Princeton University, Princeton, NJ, USA, where he is currently working toward the Ph.D. degree.

His research interests include the measurement, characterization, and data-driven modeling of power magnetics materials, as well as the design and optimization of dc–dc converters and magnetic components for point-of-load and data center applications.

Vineet Bansal received the M.S. degree in computer science from Michigan State University, East Lansing, MI, USA, in 2003.

He is currently the Lead Research Software Engineer with the Center for Statistics and Machine Learning, Princeton University, Princeton, NJ, USA, where he works on the development, optimization, scaling, and deployment of research code.

Niraj K. Jha (Fellow, IEEE) received the B.Tech. degree in electronics and electrical communication engineering from the Indian Institute of Technology (IIT), Kharagpur, India, in 1981, and the Ph.D. degree in electrical engineering from the University of Illinois at Urbana–Champaign, Champaign, IL, USA, in 1985.

He is currently a Professor with the Department of Electrical and Computer Engineering, Princeton University, Princeton, NJ, USA. He was the Associate Director of the Andlinger Center for Energy and the Environment. He has coauthored five widely used books. He has authored or coauthored more than 470 papers, among which 15 are award-winning papers. He has received 26 patents. He is co-founder of a start-up company called NeuTigers. He has given several keynote speeches in the areas of smart health care, nanoelectronic design/test, and cybersecurity. His research interests include smart health care and machine learning algorithms/architectures.

Dr. Jha is a Fellow of the Association for Computing Machinery. He was a recipient of the Distinguished Alumnus Award by IIT Kharagpur in 2014. He was the Editor-in-Chief for IEEE TRANSACTIONS ON VERY LARGE SCALE INTEGRATION (VLSI) SYSTEMS and an Associate Editor for IEEE Transactions and other journals.

Yuxin Chen (Senior Member, IEEE) received the B.S. (Hons.) degree in microelectronics from Tsinghua University, Beijing, China, in 2008, the M.S. degree in electrical and computer engineering from The University of Texas at Austin, Austin, TX, USA, in 2010, and the M.S. degree in statistics and the Ph.D. degree in electrical engineering from Stanford University, Stanford, CA, USA, in 2015.

He is currently an Associate Professor of Statistics and Data Science with the Wharton School, University of Pennsylvania, Philadelphia, PA, USA. From 2017 to 2021, he was an Assistant Professor of Electrical and Computer Engineering with Princeton University, Princeton, NJ, USA. From 2015 to 2017, he was a Postdoctoral Scholar with the Department of Statistics, Stanford University. His research interests include high-dimensional data analysis, convex and nonconvex optimization, reinforcement learning, statistical learning, statistical signal processing, and information theory.

Dr. Chen is the recipient of the Alfred P. Sloan Research Fellowship, the Google Research Scholar Award, the Princeton Graduate Mentoring Award, the AFOSR Young Investigator Award, the ARO Young Investigator Award, the ICCM Best Paper Award (Gold Medal), and the Princeton SEAS Junior Faculty Award. He was selected as the Finalist for the Best Paper Prize for Young Researchers in Continuous Optimization 2019.

Charles R. Sullivan (Fellow, IEEE) received the B.S. (Hons.) degree in electrical engineering from Princeton University, Princeton, NJ, USA, in 1987, and the Ph.D. degree in electrical engineering from the University of California, Berkeley, CA, USA, in 1996.

During his Ph.D. research, he was with Lutron Electronics, Coopersburg, PA, USA, where he designed electronic ballasts. He is currently a Professor with the Thayer School of Engineering, Dartmouth College, Hanover, NH, USA, where he is also the Director of the Power Management Integration Center. He has 43 U.S. patents and is a Co-Founder of Resonant Link, Inc., South Burlington, VT, USA. His research interests include modeling and design optimization of magnetics and other passive components for high-frequency power conversion and wireless power transfer.

Dr. Sullivan was the recipient of the IEEE Power Electronics Society Modeling and Control Technical Achievement Award in 2018 and three IEEE Power Electronics Society Prize Paper Awards.

Minjie Chen (Senior Member, IEEE) received the B.S. degree in electrical engineering from Tsinghua University, Beijing, China, in 2009, and the S.M., E.E., and Ph.D. degrees in electrical engineering and computer science from the Massachusetts Institute of Technology, Cambridge, MA, USA, in 2012, 2014, and 2015, respectively.

He is currently an Assistant Professor of Electrical and Computer Engineering and the Andlinger Center for Energy and the Environment, Princeton University, Princeton, NJ, USA. His research team developed the MagNet database, built the MagNet-AI platform, launched the MagNet Challenge, and is leading the open-source MagNet community. His research interests include high-frequency power electronics, power architecture, power magnetics, advanced packaging, data-driven methods, design automation, and design methods of high-performance power electronics for emerging and important applications.

Dr. Chen is a recipient of the IEEE Power Electronics Society (PELS) Richard M. Bass Outstanding Young Power Electronics Engineer Award, the Princeton SEAS E. Lawrence Keyes, Jr./Emerson Electric Co. Junior Faculty Award, the National Science Foundation CAREER Award, five IEEE TRANSACTIONS ON POWER ELECTRONICS Prize Paper Awards, a COMPEL Best Paper Award, an ICRA Best Poster Award, three ECCE Best Demo Awards, a 3D-PEIM Rao R. Tummala Best Paper Award, an OCP Best Paper Award, a Siebel Research Award, a C3.ai Research Award, a First Place Award of Princeton Keller Center Innovation Forum, and the MIT EECS D. N. Chorafas Ph.D. Thesis Award. He was listed on the Princeton Engineering Commendation List for Outstanding Teaching multiple times. He is the Vice-Chair of PELS TC10 Design Methodologies, and a Technical Program Committee Member of a few flagship PELS conferences including IEEE Applied Power Electronics Conference and Exposition, IEEE Energy Conversion Congress and Exposition, IEEE Workshop on Control and Modeling for Power Electronics, and IEEE International Conference on DC Microgrids.